# Three dimensional modelling of soil-plant interactions: consistent coupling of soil and plant root systems

**Inaugural-Dissertation**

zur

Erlangung des Grades

Doktor der Agrarwissenschaft

(Dr.agr.)

der

Hohen Landwirtschaftlichen Fakultät

der

Rheinischen Friedrich-Wilhelms-Universität

zu Bonn

vorgelegt im Februar 2009

von

Tom Schröder

aus

Heerlen, Niederlande

Referent: Prof. Dr. H. Vereecken
Korreferent: Prof. Dr. H. Goldbach

Tag der mündlichen Prüfung: 05.06.2009
Gedruckt bei: Graphische Betriebe, Forschungszentrum Jülich
Erscheinungsjahr: 2009
Diese Dissertation ist auf dem Hochschulschriftenserver der ULB Bonn
http://hss.ulb.uni-bonn.de/diss_online elektronisch publiziert.

This work is dedicated to my dear father
Wilhelmus A. G. Schröder (04.09.1950 - † 07.06.2006)

# Abstract

To understand how the uptake of water by roots locally affects and is affected by the soil water distribution, 3D soil-root water transfer models are needed. Nowadays, fully coupled 3D models at the plant scale, that simulate water flow along water potential gradients in the soil-root continuum, are available. However, the coupling of the soil and root system is not investigated thoroughly. In the available models the soil water potential gradient below the soil spatial discretization is neglected. Because of the non-linear behavior of the soil hydraulic conductivity, large discrepancies are expected in estimation of the soil water potential at the soil-root interface, if these local soil-root interactions are considered. This will affect the estimation of root water potentials and as such the amount of water taken up by the roots of plants.

In this thesis a microscopic analytical approach is developed that describes the soil hydraulic conductivity drop below the soil spatial discretization. The local hydraulic conductivity drop is derived and validated for a 3D soil-root water transfer model from the bulk soil to the soil-root interface. Furthermore, it was incorporated in the 3D model for the assessment of densed root architectures. Simulations showed that the total root water uptake is affected strongly by considering the local soil hydraulic conductivity drop around roots. Especially under conditions when the radial root hydraulic conductivity, regulating root water uptake, is larger than the soil hydraulic conductivity, regulating water flow in the soil. It was furthermore shown that a fine soil and root discretization was required to accurately predict soil and root water potentials. The usage of a fine soil and root discretization goes along with a considerable computational effort. Therefore a grid refinement technique was developed, based on the root architecture. Simulations performed with this refinement technique showed that the computational time was reduced largely, compared to very fine regular grids, but with maintained accuracy.

# Kurzfassung

Um zu verstehen, wie die Wasseraufnahme durch Wurzeln lokal die Wasserverteilung im Boden beeinflusst und durch diese beeinflusst wird, werden 3D-Boden-Wurzel-Wassertransfer-Modelle benötigt. Es wurden bereits vollständig gekoppelte 3D Modelle auf der Pflanzenskala entwickelt, die den Wasserfluss entlang von Wasserpotential-Gradienten innerhalb des Boden-Wurzel-Kontinuums simulieren. Die Kopplung des Boden-Wurzelsystems ist jedoch noch nicht gründlich untersucht worden. In den vorhandenen Modellen wird der Boden-Wasserpotential-Gradient unterhalb der räumlichen Auflösung des Bodens vernachlässigt. Aufgrund des nicht-linearen Verhaltens der hydraulischen Leitfähigkeit des Bodens sind sehr starke Abweichungen in der Schätzung des Boden-Wasserpotentials an der Boden-Wurzel-Grenzschicht zu erwarten, wenn diese lokalen Boden-Wurzel-Wechselwirkungen berücksichtigt werden. Dies wirkt sich auf die Schätzung des Wurzel-Wasserpotentials aus und somit auf die Wassermenge, die durch die Pflanzenwurzeln aufgenommen wird.

In dieser Arbeit wurde ein mikroskopischer analytischer Ansatz zur Beschreibung der hydraulischen Leitfähigkeitsgradienten unterhalb der räumlichen Diskretisierung des Bodens entwickelt. Der lokale Leitfähigkeitsgradient wurde für ein 3D Boden-Wurzel-Wassertransfer-Modell vom Boden zur Boden-Wurzel-Grenzschicht hergeleitet und validiert, und in ein 3D Modell zur Untersuchung von dichten Wurzelarchitekturen integriert. Anhand von Simulationen wurde gezeigt, dass die gesamte Wurzelwasseraufnahme durch die Berücksichtigung der lokalen hydraulischen Leitfähigkeitsgradienten in der näheren Wurzelumgebung stark beeinflusst wird. Dieser Einfluss war besonders stark, wenn die radiale Wurzelleitfähigkeit, die die Wurzelwasseraufnahme reguliert, größer war als die hydraulische Leitfähigkeit des Bodens, die den Wasserfluss im Boden kontrolliert. Gleichzeitig wurde gezeigt, dass eine feine Boden- und Wuzeldiskretisierung notwendig ist, um Wasserpotentiale im Boden und in den Wurzeln exakt zu beschreiben. Die Verwendung von feinen Boden- und Wurzeldiskretisierungen ist mit einem beträchtlichen Rechenaufwand verbunden. Daher wurde eine Methode zur Gitterverfeinerung entwickelt, die auf der

Wurzelarchitektur basiert. Simulationen zeigten, dass die Rechenzeit durch diese Verfeinerungsmethode stark verkürzt wurde im Gegensatz zu sehr feinen regulären Gittern. Die Genauigkeit blieb dabei unverändert.

# Contents

# Chapter 1

# Introduction

Photosynthetic absorption of carbon dioxide from the atmosphere leads to the loss of water by evaporation from the leaves of plants (transpiration). Water is absorbed from the soil by plant roots to compensate for this transpirational loss. As a consequence, a flow of water through the plant from the soil to the atmosphere occurs (Weatherley, 1982). The induced flow of water experiences frictional resistances and is therefore dependent on the hydraulic properties of the soil, of the interface between soil and root, and of the plant conducting tissues.

The root system which links the soil, where water and nutrients reside, to the above ground part of the plant, where these resources are mainly used, is complex. Roots show a remarkable ability to adapt to changes in the availability of water and nutrients, as well as to chemical properties of the soil. Root response to soil properties, in turn, affects the uptake of soil water and nutrients (Jackson *et al.*, 2000; Feddes and Raats, 2004).

Irrigation is required if the soil is incapable of providing the plant's need for water. A better understanding of the soil-plant system could help to optimize irrigation management or in the prediction of yield under water scarcity conditions. Furthermore, it helps for the assessment of pollutant fate in cropped soils or for the prediction of water uptake by natural vegetation in semi-arid and arid conditions. To deal with such problems the development of large scale hydrological models, which handle the interacting processes between plant and soil, are needed. However, to model complicated soil-plant interactions at a large scale they should first fully be understood at smaller scales. With detailed knowledge of these interactions at smaller scales effective upscale mechanisms may be found. In this study soil-plant interactions at the plant scale are investigated. A schematic of the main water fluxes entering and leaving the soil-plant system at this scale is given in Fig. 1.1.

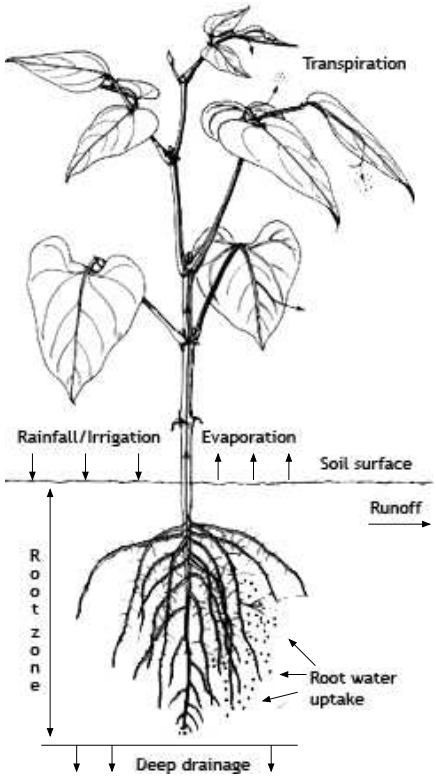


**Fig.** 1.1: Water balance at the plant scale. Transpiration of water from the leaves of a plant causes the uptake of water from the soil into the roots.

## 1.1 Water flow in soils

A natural soil develops as the interface between atmosphere and lithosphere. It is formed initially through disintegration and decomposition of rocks by physical, biological and chemical processes. The soil is divided in three phases: the solid, liquid and gaseous phase. The solid phase constitutes the soil matrix and is a mixture of mineral and organic constituents. The organization of the solid components of the soil determines the geometric characteristics of the pore spaces in which water (liquid phase) and air (gaseous phase) are transmitted and retained (Hillel, 1980).

The soil functions as a reservoir which controls the availability of water for plants influenced by rainfall/irrigation, drainage and the evaporation demand (Fig. 1.1). The reservoir is dependent of its texture and structure, moreover, of the characteristics of the root system. Water flow in the soil is generally described by models that are based on the Richards equation for variable saturated media (Richards, 1931). In this thesis single-porosity media is considered only, which means that the flow of water is not significantly affected by macropores, root channels and fractures. For the description of water flow in

non single-porosity media an extensive overview is given by Šimůnek *et al.* (2003).

Because the Richards equation is the basis equation that is used throughout this thesis a brief description of its components is given hereafter. Richard's theory combines the mass balance and the balance of momentum, the latter expressed in Darcy's law. Assuming incompressibility of water, the 3D mass balance can be written as

$$\frac{\partial \theta}{\partial t} = -\nabla \cdot \boldsymbol{F} - S \tag{1.1}$$

with $\theta$ [cm$^3$ cm$^{-3}$] the volumetric water content, $t$ [d] the time, $\boldsymbol{F}$ the volumetric flux of water [cm d$^{-1}$] and $S$ [d$^{-1}$] the sink term representing water uptake by roots. The volumetric flux is described by Darcy's law

$$\boldsymbol{F} = -K(\theta)\nabla(\psi_w) \tag{1.2}$$

where $K$ [cm$^3$ d kg$^{-1}$] is the hydraulic conductivity tensor and $\psi_w$ [kg cm$^{-1}$ d$^{-2}$] the soil water potential equal to

$$\psi_w = \psi_m + \psi_g + \psi_o \tag{1.3}$$

The water potential is the potential energy required to move an infinitesimal volume of pure free water from one area to another. The matric potential $\psi_m$ describes the amount of work due to capillary and adsorptive forces and is in most natural soils the largest component of $\psi_w$. The gravitational potential $\psi_g$ defines the amount of work due to gravitational forces, and the osmotic potential $\psi_o$ denotes the energy needed for solutes to dissolve, across a semi-permeable membrane or diffusion barrier, in the soil water. Substitution of the previous equations with $\psi_g = -\rho_w g \boldsymbol{e_z}$ and neglecting the osmotic potential yields

$$\frac{\partial \theta}{\partial t} - \nabla \cdot [K(\theta)[\nabla \psi_m - \rho_w g \boldsymbol{e_z}]] = -S \tag{1.4}$$

with $\rho_w$ [kg cm$^{-3}$] the water density, $g$ [cm d$^{-2}$] the gravitational acceleration and $\boldsymbol{e_z} = \nabla z$ the unit vector field in the vertical direction.

The soil water characteristics describe the relation between the water content, water potential and the hydraulic conductivity of a media. These characteristics are constitutive relationships that are required for evaluation of Eq. (1.4). Commonly used relationships for single-porosity media were reviewed by Leij *et al.* (1997). Eq. (1.4) can then be rewritten

as a function of $\psi_m$

$$C(\psi_m)\frac{\partial \psi_m}{\partial t} - \nabla \cdot [K(\psi_m)[\nabla \psi_m - \rho_w g \boldsymbol{e_z}]] = -S \tag{1.5}$$

with $C(\psi_m) = {}^{d\theta}/_{d\psi_m}$ [cm d$^2$ kg$^{-1}$] the volumetric water capacity. Note that the hysteresis nature of the $\psi_m$-$\theta$ relationship is neglected in this thesis.

The obtained form is called the Richards equation in potential form. An alternative form is the head form (water potential on weight basis), using the hydraulic head $H = {}^{\psi_w}/_{\rho_w g}$ [cm] instead of the water potential $\psi_w$. Replacing Eq. (1.3) by

$$H = -h - \boldsymbol{e_z} \tag{1.6}$$

where $h = -{}^{\psi_m}/_{\rho_w g}$ is the matric head and let $\boldsymbol{F}$ be equal to $-K^*(h)\nabla h$, the Richards equation in head form is given by

$$\frac{\partial \theta}{\partial t} = C^*(h)\frac{\partial h}{\partial t} = \nabla \cdot [K^*(h)[\nabla h + \boldsymbol{e_z}]] - S \tag{1.7}$$

where $C^*(h) = {}^{d\theta}/_{dh} = -\rho_w g C(\psi_m(h))$ [cm$^{-1}$] is the volumetric water capacity in head form and K$^*(h)$ the hydraulic conductivity in head form [cm d$^{-1}$]. In the remainder of this thesis we will use the Richards equation in head form and drop the $^*$ notation. Moreover, the matric water potential is denoted as the soil water potential.

The Richards equation describes water flow within the soil system. The estimated amount of water in the soil is affected by water flow in and out of the soil system. In soils where roots reside root water uptake is shown to have an enormous impact on the local depletion of water from the soil (Dunham and Nye, 1973; Li *et al.*, 2002b; Garrigues *et al.*, 2006). Dried up soil in the root zone, irrespective of rainfall/irrigation events, is rewetted again by soil moisture redistribution from the water table (capillary rise), lateral water flow from more wetter soil regions, and by more conductive roots that transfer water from wet to dry soil regions within the root zone (hydraulic lift; Jackson *et al.* (2000)).

## 1.2 Water flow in roots

The root system architecture of a plant can be regarded as the result of the accumulated effects of growth and branching responses by individual root tips and the root tissue behind these root tips to local soil conditions and the overall state of the plant (Diggle, 1988).

Root systems perform two primary functions: one is the acquisition of water and nutrients from the soil and the second is anchorage. Other functions such as storage, synthesis of growth regulators, propagation, and dispersal can be seen as secondary (Fitter, 1996). Root architectures vary greatly within and between species and many attempts have been made to classify these systems (Cannon, 1949; Weaver, 1958). The root system can be divided into a set of axes that are each derived from a meristem and are characterized by different orders: first-order (primary) axes are directly connected to the stem of the plant; second-order (secondary) axes are connected to primary axes; and so forth. Many models have been developed that describe the root architecture and their growth functions based on this hierarchial classification (Diggle, 1988; Somma *et al.*, 1998; Dunbabin *et al.*, 2002; Pagès *et al.*, 2004).

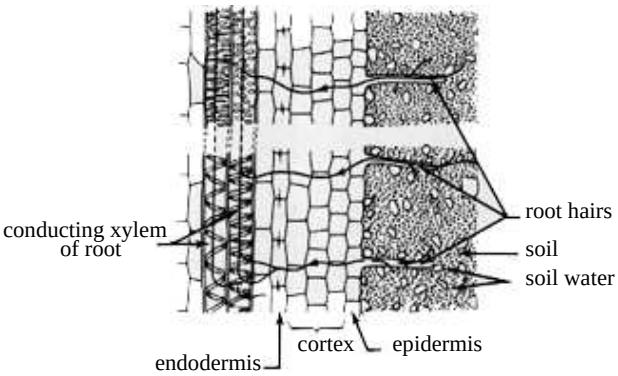


**Fig.** 1.2: Schematic of a root in the soil. Water is mainly taken up by root hairs and is transferred radially over the cortex in the xylem tissue, where it is transferred upwards to the stem of the plant.

Water movement from the soil towards and into roots and transfer from water along the roots to the above ground part of a plant is a vital process for plant existence. Roots mainly take up water by root hairs that increase the effective surface area of the root (Segal *et al.*, 2008). Water is transferred over the cortex into the xylem tissue of a root where it is transferred upwards to the stem of the plant (Fig. 1.2).

Landsberg and Fowkes (1978) described radial water flow across the root based on water potential differences between the soil-root interface and the xylem tissue, dependent on a constant radial root resistance (the resistance is related to the conductivity by its reciprocal). The flux of water that is transferred upwards through the xylem tissue was described as the xylem water potential difference in axial direction. Alm *et al.* (1992) extended the results of Landsberg and Fowkes (1978) and separated the root into segments for which they introduced a homogeneous axial resistance. Doussan *et al.* (1998a) upscaled this approach to the whole root system architecture. They assumed that the flow of water

through each part of the root system is in steady-state. This implies that the flow of water in the xylem tissue is only dependent of the axial resistances of the individual root segments and that capacitive effects of the root segments are neglected (Hunt *et al.*, 1991).

Root radial and axial resistances are highly variable (Tsuda and Tyree, 2000). They depend on plant species, the type of root branch (primary axis, secondary axis, etc.), their age, temperature and on the status of the plant and the soil. Primary roots of maize have for example less axial resistance than tertiary roots (Frensch and Steudle, 1989). Doussan *et al.* (1998b) showed that young maize roots have very high axial resistances and decrease over time when the roots get older. Lopez and Nobel (1991) showed that temperature had a large effect on root resistances in two cactus species. Furthermore, they pointed out that root resistances increased in drying soils and caused the root to act as a rectifier, such that less water was taken up. Because roots in the soil are not well accessible, basic hydraulic properties of roots are not yet adequately understood (Steudle, 2000).

## 1.3 Water flow between soil and root

It is known that water is taken up by roots in proportion to the water potential difference between soil and root and that this local flux is dependent on the hydraulic conductivity in the vicinity of and in the roots. However, there has been a long ongoing debate regarding the relative magnitude of the water flow resistance due to soil and root (Newman, 1969; Taylor and Klepper, 1975; Nobel and Cui, 1992). Several authors argued that the resistance, and as a consequence the water potential gradient, in the vicinity of roots could among other things be affected by bad soil-root contacts (Huck *et al.*, 1970; Tinker, 1976; Herkelrath *et al.*, 1977; Bristow *et al.*, 1984) or the fact that only a few roots could be active (Passioura, 1980). Experimental investigations have shown that in dry soil regions high water potential gradients between the bulk soil and soil-root interface exist and that in this case soil hydraulic properties limit the potential root water uptake (Li *et al.*, 2002b; Garrigues *et al.*, 2006). The difficulty of measuring locally the soil water status near the soil-root interface makes the experimental verification of the relative magnitude of the water flow resistance due to soil and root hard. Besides the experimental investigations, mathematical models that consider the water potential gradient near and in the roots are needed to characterize these important soil-root interactions.

The uptake of water by plant roots can be considered for different scales. The first, microscopic, scale describes the uptake of water by roots as a flux across the soil-root interface. The flux is dependent on soil and root properties, i.e. based on geometrical soil

and root parameters, on soil and root water potentials and on the soil hydraulic properties. The microscopic scale modelling approach describes radial water flow towards individual roots analytically (Gardner, 1960; Cowan, 1965; Jakobsen, 1974; De Willigen and van Noordwijk, 1987) or numerically (Hillel *et al.*, 1975; De Jong van Lier *et al.*, 2006). The microscopic expressions can be used to characterize the macroscopic root structure. The whole root structure is then described as a set of such individual roots, assumed to be regularly spaced in the soil at definable distances that may vary with the soil profile. A numerical model was developed by De Jong van Lier *et al.* (2007). Note that microscopic scale modelling approaches do not consider vertical water flow.

The second, macroscopic, scale describes the uptake of water by plant roots via an extraction term in the water flow equation (Eq. (1.7)) (Molz, 1981; Hopmans and Bristow, 2002; Feddes and Raats, 2004; Green *et al.*, 2006). The root system is assessed by its spatial distribution (e.g. root length density). The extraction functions can be categorized in three types. Type 1 considers this function to be dependent on microscopic water flow from the soil to, and through, individual roots (Nimah and Hanks, 1973). With such mechanistic models the actual plant transpiration can be related to soil and root water potentials and resistances of individual roots. It allows for compensation of water from non water stressed soil layers to water stressed soil layers. Type 2 uses semi-empirical approaches to describe the water uptake as function of the soil root density, the soil water content, and the plant transpiration (Feddes and Raats, 2004). Because the same potential plant transpiration is used for all soil layers no compensation of water from non water stressed soil layers to water stressed soil layers is possible. In order to obtain this, local water uptake mechanisms are needed (Jarvis, 1989). The choice of the compensation mechanism, as well as the extraction function, may have important consequences on the simulated water uptake dynamics and occurrence of water stress (Teuling *et al.*, 2006). Most of the models at the macroscopic scale use 1D numerical approaches to describe the Richards equation in vertical direction only. More detailed models were developed regarding the root system architecture and lead to 3D macroscopic (type 2) soil water flow models (Clausnitzer and Hopmans, 1994), where the effect of fully integrated root architecture models on soil water variability could be investigated. The disadvantage of the type 1 and 2 root water uptake models is that they do not consider the water flow within the root xylem tissue and can therefore not be used to predict phenomena like hydraulic lift. Developments regarding the root hydraulic system (e.g. Roose and Fowler, 2004) have lead to a third type of macroscopic models, so called hybrid models. Hybrid models use the microscopic approach of type 1 but integrate

this on the whole root architecture. These models consider water flow in the soil as well as in the complete root architecture. A fully coupled 3D soil-root model based on water potential differences in the soil and root system was developed by Doussan *et al.* (2006). Recently, Javaux *et al.* (2008) has extended the implementation of the coupling of this 3D soil-root water transfer model.

## 1.4 Challenges in state of the art 3D root water uptake models

In the 3D root water uptake model of Javaux *et al.* (2008), the root structure is independently coupled to the soil grid that is used for the numerical solution of the water flow equation. Therefore an approach that relates the water potentials at the grid nodes of the water transfer model and of the root model is required. The disadvantage is that the water potential at a given root node is taken to be equal to the average of the water potential at the surrounding soil nodes, thereby neglecting the water potential gradient below the soil spatial resolution, so in the vicinity of the soil-root interface. The local water potential gradient may have large influence because of the non-linear behavior of the soil hydraulic properties, especially near plant stress conditions, where soil water availability is limited. This gradient, in this thesis referred to as the hydraulic conductivity drop, is taken into account in the water flow equation and can be compensated for by using fine soil elements (Wilderotter, 2003) or by pursuing a microscopic approach from the bulk soil to the soil-root interface. When fine soil elements are used the number of degrees of freedom increase largely. As a consequence, the computational costs increase drastically. To maintain the accuracy of a fine grid but reduce the computational costs, grid refinement techniques can be applied.

## 1.5 Objectives of this study

The first general objective is to evaluate the effect of considering the local soil hydraulic conductivity drop on the estimated water uptake by plant roots, using the state of the art 3D soil-root water transfer model of Javaux *et al.* (2008). The second objective is to optimize this 3D model in terms of accuracy and computational speed. The different issues investigated in this thesis are:

1. to build and assess a microscopic analytical approach that estimates the local hydraulic conductivity drop, below the soil spatial discretization, from the bulk soil to

the soil-root interface to be used in the 3D soil-root water transfer model of Javaux *et al.* (2008);

2. to incorporate and assess the analytical approach in the model of Javaux *et al.* (2008) for multiple roots using different modelling techniques;

3. to develop a grid refinement method for the 3D soil-root water transfer model to be computational quicker and without loosing accuracy compared to fine regular soil grids.

## 1.6 Thesis outline

Chapters 2 to 4 are based on papers that have been or will be published independently in international journals. Consequently, some duplication is unavoidable.

In chapter 2 a microscopic analytical approach is developed that describes the water potential gradient below the soil spatial discretization from the bulk soil to the soil-root interface. The analytical approach is validated by numerical means and with these tools quantification of the local soil hydraulic conductivity drop is assessed. Furthermore, the analytical approach is implemented in the 3D soil-root water transfer model to be used for single roots and evaluated for different soil-root scenarios. Comparisons of a single root scenario for different soil discretizations with and without considering the local conductivity drop are performed. First to show the effect on the estimated soil-root interface water potential and secondly for validation purposes.

Chapter 3 deals with the implementation of the microscopic analytical approach for multiple roots as is usually the case for densed root architectures within a soil column. Three different modelling methods, based on modelling assumptions used by authors in this research field, are considered to deal with the microscopic analytical approach of chapter 2. The multiple root methods are assessed for different soil-root scenarios, especially in dry soil regions, and compared with the average method proposed by Javaux *et al.* (2008), moreover to a reference scenario using a fine regular soil grid.

Chapter 4 deals with the development of a grid refinement approach to be used for 3D soil-root water transfer models. As root water uptake is one of the main contributors to changes in the soil status, root information is used to refine the soil grid *a priori*, either in a static or dynamic way. Static *a priori* refined grids are compared for a soil-root scenario with coarse grid configurations and with a reference scenario using a fine soil discretization. Furthermore, static *a priori* grids are compared and validated with a well

recognized *a posteriori* refinement method. Lastly, dynamic *a priori* refinement is assessed.

In Chapter 5 the conclusions are drawn and a perspective into future research is given.

# Chapter 2

# Effect of the local soil hydraulic conductivity drop on root water uptake using a 3D plant scale model*

## 2.1 Objectives

The objectives in this chapter are to quantify the hydraulic conductivity drop below the soil spatial resolution using an analytical approach, and to validate it by numerical means. Furthermore, the implementation of the analytical approach within a voxel of a 3D soil-root water transfer model will be evaluated.

## 2.2 Introduction

The understanding of the uptake of water by roots is of importance for a variety of environmental and agricultural purposes, such as yield prediction under water scarcity conditions, irrigation management and assessment of pollutant fate in cropped soils. The first type of models used for prediction of these processes are 1D macroscopic water flow models using extraction functions. These extraction functions use semi-empirical approaches to describe the water uptake as function of the soil root density, the soil water content, and the plant transpiration (Feddes and Raats, 2004). However, these models do not consider the water flow within the root system and can therefore not be used to predict phenomena

*adapted from T. Schröder, M. Javaux, J. Vanderborght, B. Körfgen, and H. Vereecken (2008). Effect of local soil hydraulic conductivity drop using a 3D root water uptake model. Vadose Zone Journal, 7, 1089-1098

like hydraulic lift (Jackson *et al.*, 2000). Furthermore, the effects of the vertical water distribution and water scarcity on local root water uptake is not directly considered, but must be described using empirical relations that describe local water uptake compensation mechanisms (Jarvis, 1989). The choice of the compensation functions may have important consequences on the simulated water uptake dynamics and occurrence of water stress (Teuling *et al.*, 2006). The second type of models describe microscopically water flow towards roots (Gardner, 1960; Cowan, 1965; Hillel *et al.*, 1975; De Willigen and van Noordwijk, 1987; De Jong van Lier *et al.*, 2006) but they do not consider vertical water flow variability. Personne *et al.* (2003) proposed a model of vertical 1D water redistribution integrating water transfer from soil to roots, but does not consider fully integrated 3D root models.

More detailed models were developed regarding root system architectures (Pagès *et al.*, 1989) and their hydraulics (Doussan *et al.*, 1998a). Furthermore, 3D soil models (Clausnitzer and Hopmans, 1994) were developed, where the effect of fully integrated root models on soil water variability could be investigated. The disadvantage of these 3D models was again the semi-empirical extraction functions. Detailed modeling of the hydraulics in root systems lead to fully coupled 3D soil-root models based on water potential differences in the soil and root (Doussan *et al.*, 2006). Recently, Javaux *et al.* (2008) has extended the implementation of the coupling of this 3D soil-root flow model. Opposed to the model of Doussan *et al.* (2006) the root structure is independently coupled to the soil grid that is used for the numerical solution of the water flow equation. Therefore, an approach that relates the water potentials at the grid nodes of the water flow model and of the root model is required.

In the model of Javaux *et al.* (2008) the water potential at a given root node is taken to be equal to the average of the water potential at the surrounding soil nodes, thereby neglecting the potential drop in the vicinity of the soil-root interface. This potential drop may have large influence because of its non-linear behavior, especially under plant stress conditions, where soil water availability is scarce. This drop is taken into account in the Richards equation and can be compensated for by using smaller soil elements (Wilderotter, 2003) or by pursuing an analytical approach from the bulk soil to the soil-root interface. The analytical approach at the voxel scale is a microscopic process. The solution proposed in this thesis, to fulfill the conditions imposed by the 3D plant scale model, is an extension to solutions proposed by previous researchers (Cowan, 1965; De Willigen and van Noordwijk, 1987; De Jong van Lier *et al.*, 2006).

## 2.3 Theory

### 2.3.1 Analytical model: water flow from bulk soil to soil-root interface

Many 2D analytical approaches have been made in the past to describe water flow to root nodes (Gardner, 1960; Cowan, 1965; Jakobsen, 1974; De Willigen and van Noordwijk, 1987; De Jong van Lier *et al.*, 2006). The differences lie in the approximations and applied boundary conditions. The domain for a 2D radial analytical approach is given in Fig. 2.1 and was first introduced by Gardner (1960).

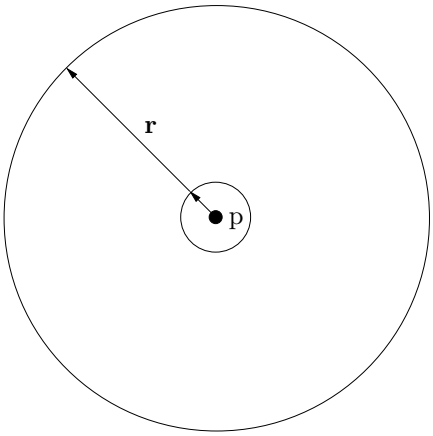


**Fig.** 2.1: 2D radial domain of the microscopic model. Outer circle represents the bulk soil with a radius $r_{out}$ from root node p to the outer circle. Inner circle represents the soil-root interface with radius $r_{root}$ from root node p to the inner circle.

To evaluate the Richards equation in the 2D domain, the radial form without gravity is (see also Schröder *et al.*, 2007)

$$\frac{\partial \theta}{\partial t} = \frac{1}{r}\frac{\partial}{\partial r}(rK(h,\theta)\frac{\partial h}{\partial r}) = -\frac{q}{r} - \frac{\partial q}{\partial r} \tag{2.1}$$

where $q$ [L T$^{-1}$] is the Darcy's flow (a flux density) denoted by $q = -K(h,\theta)\frac{\partial h}{\partial r}$, $h$ [L] the water potential on weight basis (pressure head), $r$ [L] the radial coordinate and $t$ [T] the time. The volumetric water content $\theta$ [L$^3$ L$^{-3}$] and the hydraulic conductivity $K$ [L T$^{-1}$] are soil characteristics.

This equation can be linearized using the matric flux potential

$$\Phi_{h_c} = \int_{h_{-\infty}}^{h_c} K(h)dh \tag{2.2}$$

where $h_c$ is the current water potential and $h_{-\infty}$ the lower integral boundary. In matric

flux potential form Eq. (2.1) transforms into

$$\frac{\partial\theta}{\partial t} = \frac{1}{r}\frac{\partial\Phi}{\partial r} + \frac{\partial^2\Phi}{\partial r^2} \tag{2.3}$$

Under flux and water potential type boundary conditions at the inner ($r_{root}$) and outer edges ($r_{out}$) representing the bulk soil, and under steady rate behavior, i.e. $\frac{\partial\theta}{\partial t}$ = constant, it yields

$$\Phi(r) = \Phi_{r_{out}} + (q_{root}r_{root} - q_{out}r_{out})\left(\frac{{}^{r^2}/_{r_{root}^2}}{2(1-\rho^2)} + \frac{\rho^2}{1-\rho^2}\left(\ln\frac{r_{out}}{r} - \frac{1}{2}\right)\right) +$$

$$+ q_{out}r_{out}\ln\frac{r}{r_{out}} \tag{2.4}$$

with $\rho = {}^{r_{out}}/_{r_{root}}$. In equilibrium, i.e. the volumetric water content is constant and the time derivative equals zero,

$$q_{out} = q_{root}\frac{r_{root}}{r_{out}} \tag{2.5}$$

and the Cowan (1965) approach is obtained. In case of vanishing flux, i.e. no water is extracted from the cylinder with radius $r_{out}$,

$$q_{out} = 0 \tag{2.6}$$

and the approach of De Willigen and van Noordwijk (1987) is obtained.

Under plant stress conditions, $|h \geq h_{lim}|$, a water potential instead of a flux is imposed at the soil-root interface which finally yields

$$\Phi(r) = (\Phi_{r_{out}} - \Phi_{r_{root}} + q_{out}r_{out}\ln\frac{1}{\rho})\frac{{}^{r^2}/_{r_{root}^2} - 1 + 2\rho^2\ln{}^{r_{root}}/_{r}}{\rho^2 - 1 + 2\rho^2\ln{}^{1}/_{\rho}} + q_{out}r_{out}\ln\frac{r}{r_{root}} + \Phi_{r_{root}} \tag{2.7}$$

where $\Phi_{r_{root}}$ tends to go to zero and may be neglected. Details about the derivation of Eqs. (2.4) and (2.7) are given in Appendix A.

### 2.3.2 3D numerical water flow model in soil and roots: R-SWMS

The model of Javaux *et al.* (2008), R-SWMS, consists of two interacting systems: the soil and the root architecture. For both systems a set of equations is solved in terms of water potential and both are coupled via the sink term $S$ in the Richards equation.

Boundary conditions for the plant root system can be given in terms of transpiration or water potential at the root collar, and soil water potential at the soil-root interface to solve the water potential and flux distributions in the xylem. From this a soil-root radial water flux $J_r$ [$L^3$ $T^{-1}$] can be derived

$$J_r = L_r(h_{interface} - h_{xylem}) \tag{2.8}$$

where $L_r$ is the radial root conductance [$L^2$ $T^{-1}$] and $h$ represents the water potential at the soil-root interface and in the xylem respectively. The water potential at the soil-root interface is acquired by a distance-based average of the water potential in the surrounding soil nodes

$$h_{interface} = \frac{\sum_{i=1}^{8} h_i \frac{1}{dist_i}}{\sum_{i=1}^{8} \frac{1}{dist_i}} \tag{2.9}$$

where *dist* is the distance calculated from the root node $p$ to a soil node $i$ (Fig. 2.2). The sink term [$T^{-1}$] of a soil voxel can now be defined as

$$S_j = \frac{\sum_{k=1}^{n_j} J_{r,k}}{V_j} \tag{2.10}$$

where the numerator represents the sum of all the radial soil-root fluxes of the $n_j$ root nodes located inside a soil voxel $j$ and $V_j$ [$L^3$] is the volume of the $j^{th}$ soil voxel. The sink term is distance-based distributed upon the soil nodes $i$ representing the bulk soil

$$S_i = S_j \frac{\frac{1}{dist_i}}{\sum_{k=1}^{8} \frac{1}{dist_k}}, \qquad \text{for } i = 1, \ldots, 8 \tag{2.11}$$

Initially the root system is solved with the initial soil water potential as a boundary condition at the soil-root interface. With the generated sink term, the water flow equation is solved, after which the root system is solved again until both systems fulfill tolerance criteria for the soil, in terms of water potential and water content, and for the root, in terms of water potential.

### 2.3.3 Implementation of the hydraulic conductivity drop at the voxel scale

Implementation of the 2D analytical approach, describing the water potential gradient between the bulk soil and soil-root interface, in R-SWMS is achieved by defining the

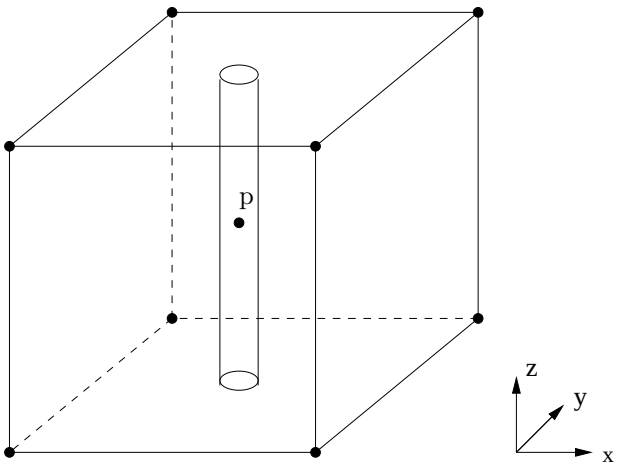


**Fig.** 2.2: A soil voxel with its soil nodes (full dots). A vertical orientated root with root node p is positioned in the soil voxel.

geometrical domain and the boundary conditions at the voxel scale. A 3D analytical solution of the Richards equation in a soil voxel can be obtained by multiplying a linearized analytical solution for a 2D radial coordinate system with a linearized analytical solution for the 1D axial component. We assume, for simplicity, that the root is orientated in axial direction in the middle of the voxel and that, as a consequence, the main influence on root water uptake is exerted by the horizontal component.

To reduce computational times the analytical approach in axial direction is interchanged by an averaging procedure. Soil water potentials and fluxes in the corner nodes of the cube are averaged upon the corner nodes of the rectangular cross-section at the axial height of root node $p$ (Fig. 2.3A). The outer boundary conditions at the bulk soil (Fig. 2.3B) are obtained by averaging the soil variables in the corner nodes of the rectangular cross-section upon the intersection points of the outer circle with the edges of the voxel, while the inner boundary conditions are defined at the soil-root interface.

## 2.4 Methodology

### 2.4.1 Effect of the hydraulic conductivity drop in the bulk soil around a root

The analytical approaches in Eqs. (2.4) and (2.7) are compared with a numerical finite difference approach for root water uptake. The finite difference method is implicitly applied to the partial derivatives of Eq. (2.1), analogue to the implementation in the WAVE model of Vanclooster *et al.* (1996). The hydraulic conductivities are averaged using the

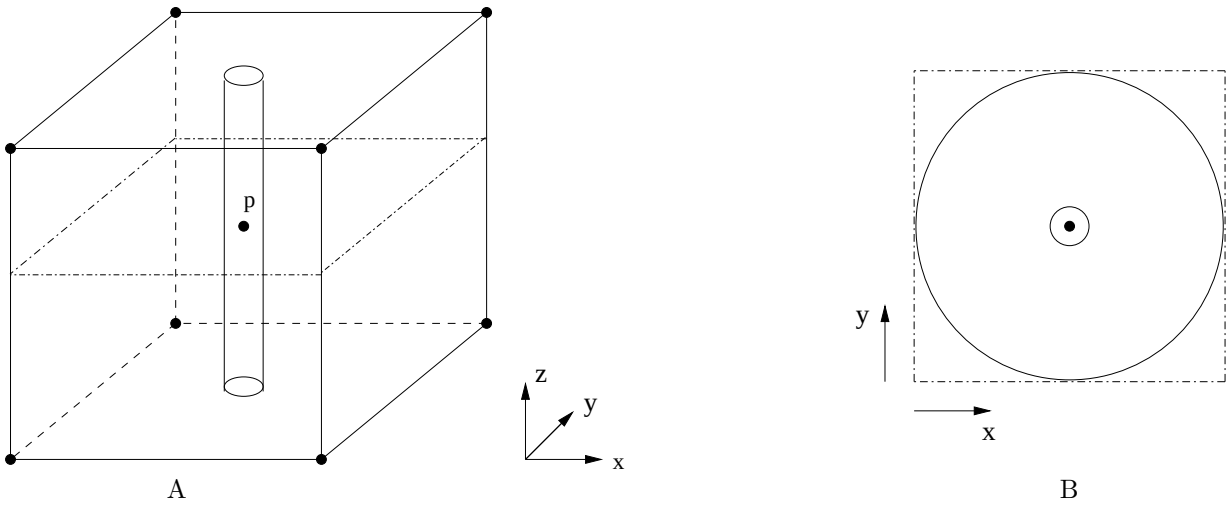


**Fig.** 2.3: **A**: A soil voxel with its soil nodes (full dots). A vertical orientated root with root node p is positioned in the middle of the soil voxel. **B**: Rectangular cross-section at the axial height of root node p (full dot). Within the rectangular cross-section the 2D radial domain, where the outer circle represents the bulk soil and the inner circle the soil-root interface.

arithmetic mean. To maintain mass conservation the Celia-approach (Celia *et al.*, 1990) is applied to the mixed form of the Richards equation. Furthermore, the non-linear terms are evaluated using a Newton-Raphson iterative method. In matrix form a tridiagonal system of linear equations is obtained, which is solved using the Thomas algorithm after applying flux or water potential type boundary conditions.

With this tool the hydraulic conductivity drop over time between the soil-root interface and bulk soil is investigated for different soil types. Therefore, two scenarios are investigated for which the inner root boundary condition $q_{root}$, associated with the climatic demand, differs. In both scenarios the initial water potential is set to -100 cm, the limiting water potential $h_{lim}$ at plant stress conditions and the integral boundary value $h_{-\infty}$ are equal to -15000 cm. The initial time increment is set to $5 \cdot 10^{-3}$ d and is automatically adjusted based on water balance errors. The radial distance from soil-root interface to bulk soil is subdivided in 200 elements based on a logarithmic scale to create smaller elements near the root.

Flux density values at the inner root ($q_{root}$), for single root segments in variable dense root structures, were investigated by De Jong van Lier *et al.* (2006) and ranged from $O(10^{-1})$ to $O(10^{-0})$ cm d$^{-1}$. We chose to perform a simulation with a low climatic demand $q_{root} = 0.1$ cm d$^{-1}$ and a second simulation with a higher climatic demand $q_{root} = 0.5$ cm d$^{-1}$. Assuming in a soil voxel of 1 by 1 by 1 cm a single root segment with a root area $A_r = 2\pi r_{root} l_r$, where the root radius $r_{root}$ equals $5{\cdot}10^{-2}$ cm and the root segment length

$l_r$ equals 1 cm, a total water flux at the root collar, $J_c = q_{root} A_r$, of respectively $3.14{\cdot}10^{-2}$ and $1.57{\cdot}10^{-1}$ cm$^3$ d$^{-1}$ is obtained. The soil surface area $A_p$ of this voxel equals 1 cm$^2$ and a potential transpiration rate, $T_p = {}^{J_c}/_{A_p}$ [cm d$^{-1}$], of equal height as the total water flux at the root collar was acquired. The latter value is rather high but may be realistic for transpiration rates at midday or during the early afternoon.

The flux density boundary condition at the outer edge was arbitrarily set to a value unequal to zero, $q_{out} = q_{root}({}^{r_{root}}/_{2r_{out}})$, and not in equilibrium with the flux density at the inner root.

The soil properties, the hydraulic conductivity $K$ as well as the volumetric water content $\theta$, are obtained via the Mualem-Van Genuchten parameterization (Van Genuchten, 1980)

$$\begin{aligned} \Theta &= \left[\frac{1}{1+(\alpha h)^n}\right]^m = \frac{\theta-\theta_r}{\theta_s-\theta_r} \\ K(\Theta) &= K_s \Theta^{\lambda}[1-(1-\Theta^{1/m})^m]^2 \\ m &= 1-\frac{1}{n} \end{aligned} \tag{2.12}$$

where $\Theta$ is the normalized water content and $\theta_r$ and $\theta_s$ indicate residual and saturated values of the water content. The saturated soil hydraulic conductivity is denoted by $K_s$, and $\alpha$, $\lambda$ and $n$ are soil parameters. In order to describe $K-\theta-h$ relationships soil specific data need to be provided, as is done by Wösten *et al.* (2001) for soils from the Dutch Staring series. Three of these soils are listed in Table 2.1. The soil hydraulic conductivity and the

**Table** 2.1: Mualem-Van Genuchten parameters for three soils from the Dutch Staring series.

| Staring soil ID | Textural Class | $\theta_r$ (cm$^3$ cm$^{-3}$) | $\theta_s$ (cm$^3$ cm$^{-3}$) | $K_s$ (cm d$^{-1}$) | $\alpha$ (cm$^{-1}$) | $\lambda$ | n |
|---|---|---|---|---|---|---|---|
| B3 | sand | 0.02 | 0.46 | 15.42 | 0.0144 | -0.215 | 1.534 |
| B11 | clay | 0.01 | 0.59 | 4.53 | 0.0195 | -5.901 | 1.109 |
| B13 | loam | 0.01 | 0.42 | 12.98 | 0.0084 | -1.497 | 1.441 |

soil water content distribution for these soils are depicted in Fig. 2.4.

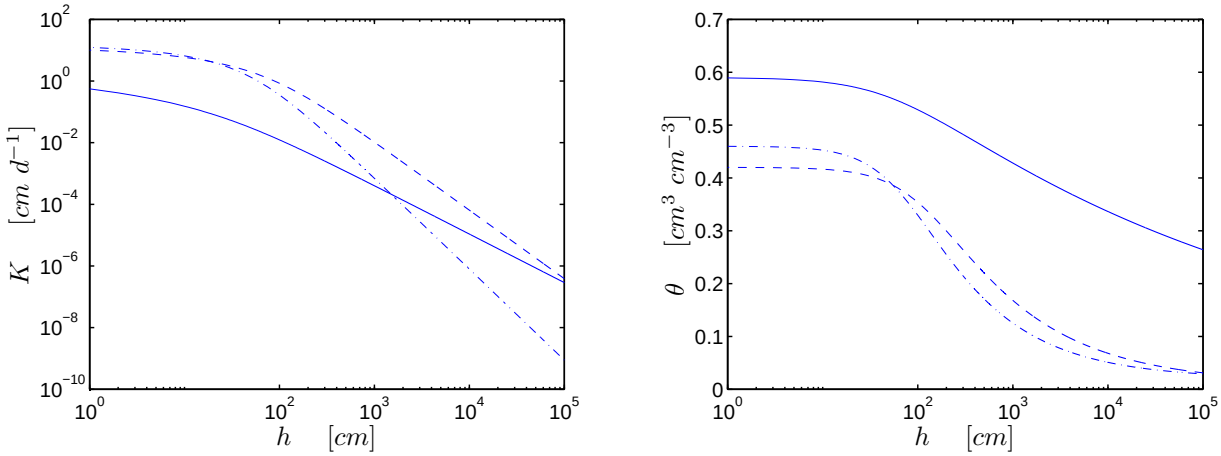


**Fig.** 2.4: The soil hydraulic conductivity (left) and soil water content (right) as function of the absolute water potential for the clay (solid line), loam (dashed line) and sandy soil (dashed-dotted line) from Table 2.1.

### 2.4.2 Effect of the hydraulic conductivity drop in a 3D soil-root water transfer model

Incorporation of the water potential gradient in the bulk soil around roots will affect root water uptake and therefore the behavior of the total soil-root system. Two different scenarios were defined (Table 2.2), considering the hydraulic conductivity drop (analytical approach) and not considering the hydraulic conductivity drop (average approach), for which R-SWMS was assessed in terms of

- water potential at the soil-root interface, at the bulk soil and in the xylem
- radial water flow from the soil-root interface to the xylem
- total water flow at the root collar

If the hydraulic conductivity drop is taken into account, the boundary conditions for the analytical approach have to be defined clearly in terms of R-SWMS output. At the outer edge of a voxel with a root segment (bulk soil) a water potential and flux density are imposed. The water potential in the soil nodes of the voxel are obtained by the Richards equation. The corresponding flux in these nodes is obtained by summation of the Darcy's flow toward each soil node from the surrounding soil nodes. At the soil-root interface a flux density equal to the radial flux from Eq. (2.8), divided by the root surface, is imposed.

In the two different scenarios only water flow was simulated without any bio-chemical influences. No root growth and no solute uptake were considered. For sake of simplicity,

we simulated a very simple root structure made of one vertical root (with length 8 cm), positioned in the center of a soil voxel and in the middle of a soil column (at $r = 0$) with dimensions 9 by 9 by 12 cm. An initial pressure head of -2000 cm throughout the soil column was prescribed, corresponding to a 67% soil moisture. At the top and bottom of the soil domain a no flux boundary condition (BC) was imposed (no rainfall/irrigation and no free drainage). The soil was parameterized with the Mualem-Van Genuchten functions (Table 2.1) and considered homogeneous. The soil was discretized in voxels of 1 by 1 by 1 cm, similarly the root segments with a length $l_r$ of 1 cm. At the root collar a time-independent water potential was imposed and the hydraulic properties for the root segments (from Doussan *et al.*, 2006) were considered constant with time (see Table 2.2). The radial root conductance is defined as $L_r = L_r^* A_r$ [cm$^2$ d$^{-1}$], where $L_r^*$ [d$^{-1}$] is the radial conductivity and $A_r$ the root area with $r_{root} = 5{\cdot}10^{-2}$ cm. The axial root conductance $K_h$ [cm$^3$ d$^{-1}$] regulates the water flow in the xylem.

The radial soil-root water flow (Eq. (2.8)) is dependent of the radial root conductance and of the difference in water potential at the soil-root interface and in the xylem. The impact on soil water variability by an increase in radial root conductivity was shown by Javaux *et al.* (2008). Because of its importance a first scenario with a low $L_r^*$ value and a second scenario with a higher $L_r^*$ value were defined. In the latter case the radial root conductivity was increased 5-fold.

**Table** 2.2: Two scenarios with their soil and root properties and boundary conditions (BC) for the R-SWMS comparison with and without incorporation of the hydraulic conductivity drop.

| Scenario | Soil texture | Root properties | | BC soil | BC root |
|---|---|---|---|---|---|
| | | $L_r^*$ [d$^{-1}$] | $K_h$ [cm$^3$ d$^{-1}$] | [cm d$^{-1}$] | collar [cm] |
| Low $L_r^*$ | clay | $1.73{\cdot}10^{-4}$ | $4.32{\cdot}10^{-2}$ | zero flux top/bottom | -2700 |
| Higher $L_r^*$ | clay | $8.64{\cdot}10^{-4}$ | $4.32{\cdot}10^{-2}$ | zero flux top/bottom | -2700 |

### 2.4.3 Validation scenario: mesh refinement

The accuracy of the different approaches was assessed by comparing simulations for different spatial discretizations. For a smaller discretization, the drop in water potential and hydraulic conductivity toward the root segment is better represented by the Richards equation in R-SWMS. The water potentials calculated at the soil nodes surrounding the root segment are expected to converge to the water potentials at the soil-root interface. Both the lower and higher radial root hydraulic conductivity scenarios of the previous section

were assessed for different soil and root discretizations, with and without considering the hydraulic conductivity drop. The discretization size ranged linearly from 0.5 by 0.5 by 0.5 cm to 4 by 4 by 4 cm. Furthermore, a reference scenario with element size 0.2 by 0.2 by 0.2 cm was simulated.

## 2.5 Results

### 2.5.1 Effect of the hydraulic conductivity drop in the bulk soil around a root

#### Spatial effect

Analytical and numerical solutions for three different soil types are compared for the higher climatic demand scenario ($q_{root} = 0.5$ cm d$^{-1}$) only, in Figs. 2.5 and 2.6.

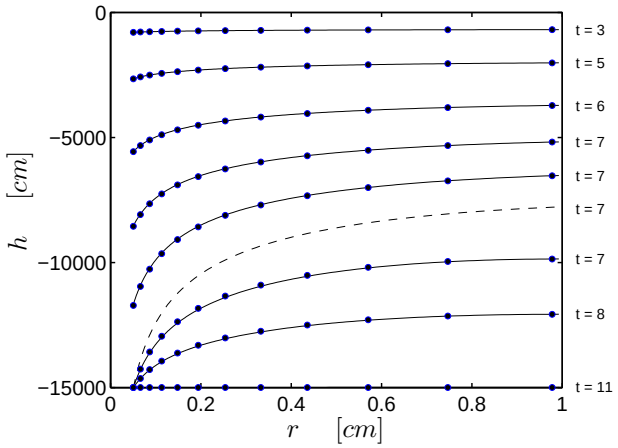


**Fig.** 2.5: Water potential distribution over time in a clay soil for the higher climatic demand scenario. A comparison is shown between the analytical solution (dots) and the numerical finite difference solution (solid line). The dashed line resembles the limiting water potential at which plant stress occurs. The simulation time is in days.

The analytical solution for all soil types approximates the numerical model very well. The relative error is maximal (about 5%) in the sandy soil measured at the moment the soil water potential reached limiting conditions and close to the soil-root interface. The mean relative error, though, over the total water potential distribution at this time was lower than 1%. The relative error for the clay and loamy soil, for all time sections, was smaller than 1% as well.

Similar results were obtained for the water content profiles. Because of the steady-rate assumption that is used to obtain the analytical solution, water content profiles dependent

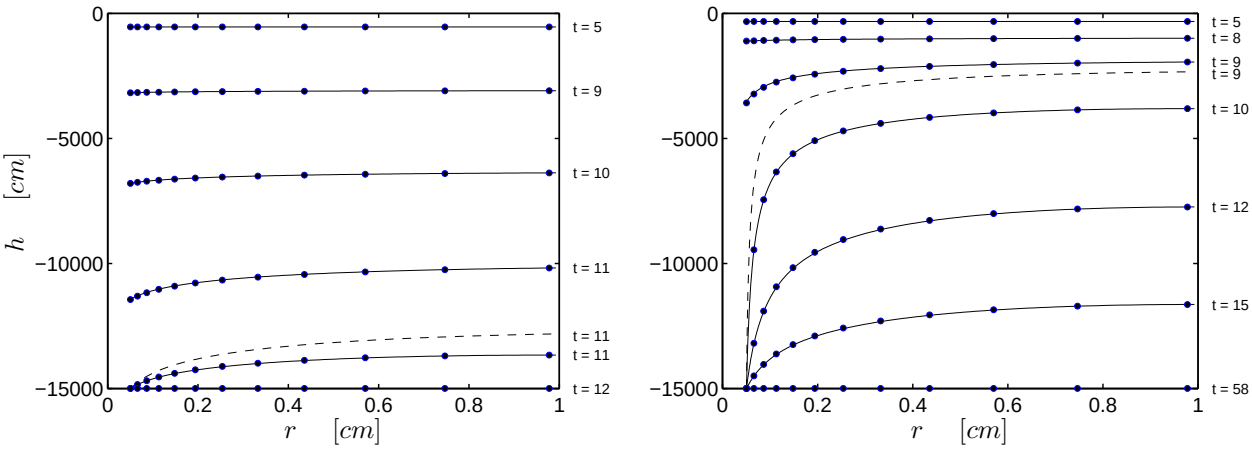


**Fig.** 2.6: Water potential distribution over time in a loamy soil (left plot) and a sandy soil (right plot) for the higher climatic demand scenario. Comparisons are shown between the analytical solutions (dots) and the numerical finite difference solutions (solid line). The dashed lines resemble the limiting water potential at which plant stress occurs. The simulation time is in days.

of time were supposed to be parallel. After the onset of plant stress conditions, and the switch from a flux to water potential type boundary condition, this steady rate assumption was violated. The water potential and the water content at the soil-root interface did not change with time anymore. Therefore, the water potential and soil water content profiles could no longer have a parallel course in the vicinity of the soil-root interface. Nevertheless, the analytical solution stayed close to the numerical solution since the changes in soil water content were small. Finally, an uniform water potential profile equal to the limiting water potential was obtained.

### Temporal effect

Fig. 2.7 shows the hydraulic conductivity over time at the soil-root interface and at the bulk soil for the three soils. The hydraulic conductivity drop between the bulk soil and soil-root interface was the largest in the sandy soil and at the moment of plant stress, where the soil-root interface hydraulic conductivity was constant. The conductivity drop in the low climatic demand scenario was a factor of 25 in the sandy soil, whereas in the clay and loamy soil hardly a drop, smaller than 1.5, could be noticed. If the demand is increased 5-fold a hydraulic conductivity drop in the sandy soil of factor 250 can be observed. The clay soil had a 3-fold drop and the loamy soil a 1.5-fold drop in hydraulic conductivity between the bulk soil and soil-root interface. The hydraulic conductivity drop strongly depends not only on the climatic demand, but also on the soil parameters $\alpha$, $\lambda$ and $n$

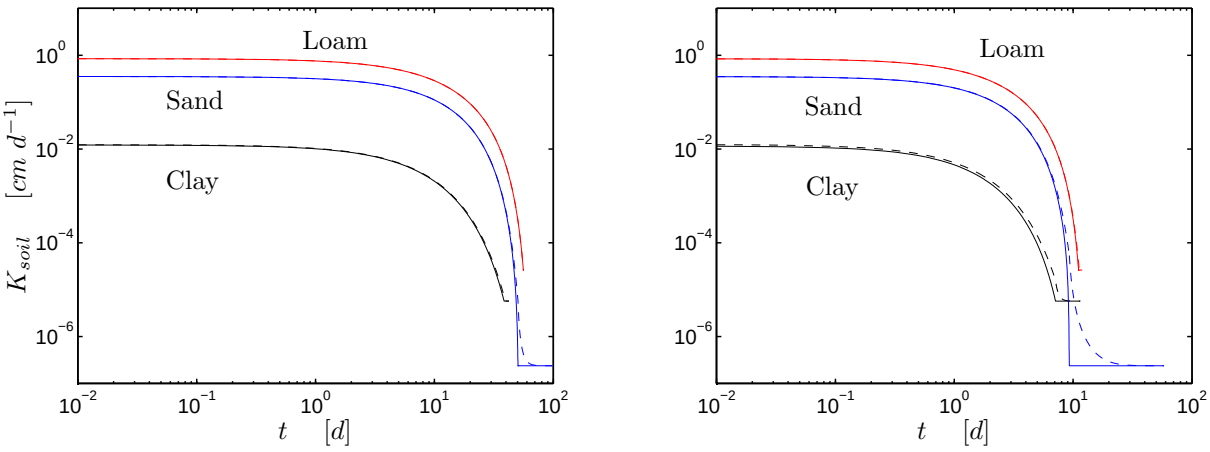


**Fig.** 2.7: Soil hydraulic conductivity over time at the soil-root interface (solid line) and at the bulk soil (dashed line) for a clay (black line), loam (red line) and sandy soil (blue line). Left graph: lower climatic demand scenario, $q_{root} = 0.1$ cm d$^{-1}$. Right graph: higher climatic demand scenario, $q_{root} = 0.5$ cm d$^{-1}$.

determining the steepness of the $K - h$ relationship.

Noticeable is the shift in time of the moment of plant stress. In case where the demand was higher, and larger water potential gradients were created, the soil reached limiting conditions earlier than in the lower climatic demand scenario. Furthermore, the moment of stress occurrence varied for the individual soils dependent on their soil hydraulic properties. If the hydraulic conductivity drop was not considered, so the hydraulic conductivity at the soil-root interface equaled the bulk soil hydraulic conductivity, it took a much longer time to reach limiting conditions, even for the low climatic demand where not so large soil hydraulic water potential gradients were observed.

### 2.5.2 Effect of the hydraulic conductivity drop in a 3D soil-root water transfer model

Root water uptake was assessed for R-SWMS for the case where the hydraulic conductivity drop was considered and for the case where it was not taken into account. Note that for all simulations, performed during one day with an initial time increment of $5{\cdot}10^{-3}$ d, the mass balance for soil and root water transfer was reduced rapidly below 1% error after initialization of the simulation.

For the low and higher radial root conductivity scenarios (Table 2.2) the water potential at the soil-root interface, at the soil voxel nodes surrounding the root segment (bulk soil), and in the xylem was evaluated as function of the rooting depth in Figs. 2.8 and 2.9.

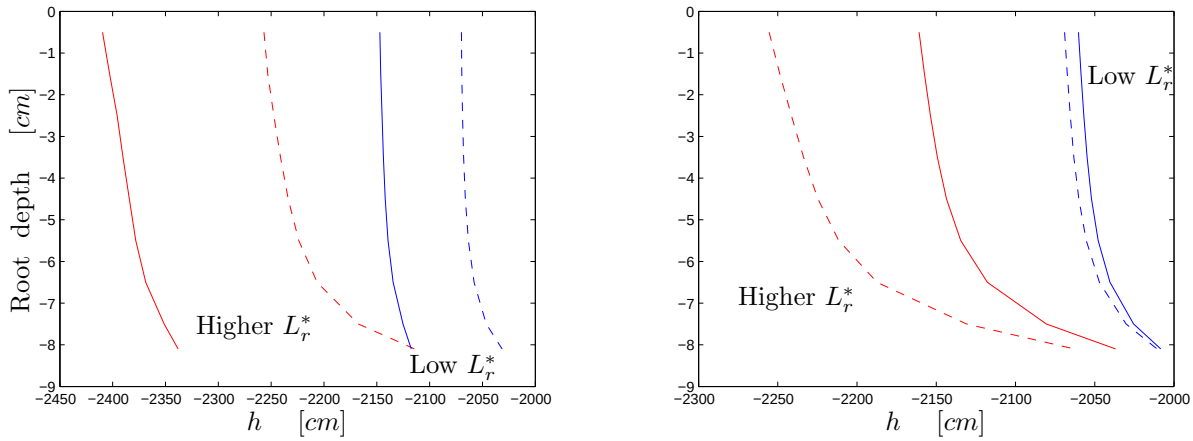


**Fig.** 2.8: Left graph: water potential at the soil-root interface as function of rooting depth. Right graph: bulk soil water potential as function of rooting depth. Without conductivity drop (dashed line) and with conductivity drop (solid line). The low $L_r^*$ scenario is denoted by the blue lines, the higher $L_r^*$ scenario by the red lines.

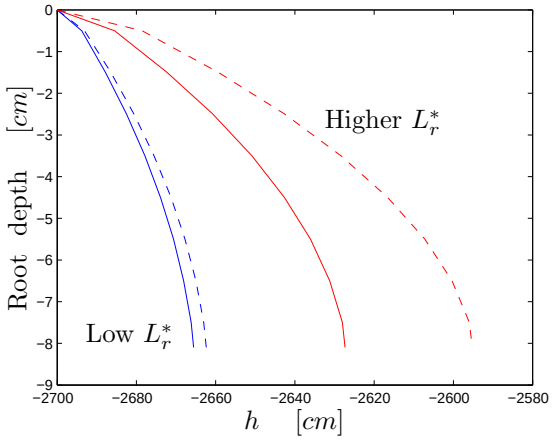


**Fig.** 2.9: Xylem water potential as function of rooting depth. Without conductivity drop (dashed line) and with conductivity drop (solid line). The low $L_r^*$ scenario is denoted by the blue lines, the higher $L_r^*$ scenario by the red lines.

The left graph of Fig. 2.8 shows, for the low radial root conductivity scenario, an average increase of 3.3% in absolute water potential at the soil-root interface considering the hydraulic conductivity drop around the root, compared with not considering the hydraulic conductivity drop. Furthermore, under the same soil and root collar boundary conditions the absolute water potential at the soil-root interface increased about 7% with a 5-fold increase in radial root conductivity.

Changes in bulk soil water potential (right graph of Fig. 2.8) were relatively small. In the low $L_r^*$ scenario, the change between considering and not considering the hydraulic

conductivity drop was smaller than 1% and only about 3.5% in the higher $L_r^*$ scenario.

The xylem water potential distribution in Fig. 2.9 illustrates that in the low $L_r^*$ scenario the xylem water potential is slightly different for both methods with and without considering the hydraulic conductivity drop. This effect can be attributed to the large axial conductance in the xylem opposed to the low radial root conductance. An increase in radial root conductivity in the higher $L_r^*$ scenario reduced the difference in conductance between an axial and radial root segment. This affects the xylem water potential when incorporating the local hydraulic conductivity drop as opposed to not considering this drop. The change, however, is not significant as it is much less than 1% in the low $L_r^*$ scenario and about 1% in the higher $L_r^*$ scenario. These errors, though, are very much dependent on the boundary conditions imposed at the root collar and on the ratio of radial and axial root hydraulic conductance.

A change in water potential at the soil-root interface and in the xylem will also cause a change in radial soil-root water flow following Eq. (2.8) (not shown). In the low $L_r^*$ scenario a relative average change of 14% was observed, whereas in the higher $L_r^*$ scenario an approximately 50% difference was observed between not considering and considering the hydraulic conductivity drop. This may be explained by assessing the hydraulic conductivities of the soil and root. In the low $L_r^*$ scenario the radial root hydraulic conductivity times the length of the resistive pathway ($r_{root}$) is lower than the soil hydraulic conductivity for the observed water potential range (Fig. 2.4). This implies that the root resistance is larger than the soil resistance and that water fluxes between soil and xylem are determined by the lower root hydraulic conductivity. When the radial root conductivity increases 5-fold the soil hydraulic conductivity becomes the limiting parameter. Changes in water potential at the soil-root interface, due to incorporation of the hydraulic conductivity drop, affect root water uptake now largely.

The water potential distribution throughout the soil was affected by the water potential at the soil-root interface, in the xylem, and the corresponding radial soil-root flux. Fig. 2.10 shows the water potential distribution throughout the soil. In the higher $L_r^*$ scenario a larger change is observed than in the low $L_r^*$ scenario, with a maximum relative error, at the closest soil node to the root segment (bulk soil), of about 4%. Dependent on soil and root boundary conditions and hydraulic properties the water potential distribution in the soil may be greatly affected, which means that estimated water fluxes will be affected. Another noticeable observation in Fig. 2.10 is that the estimated absolute soil water potential at the soil nodes was less in case where the hydraulic conductivity

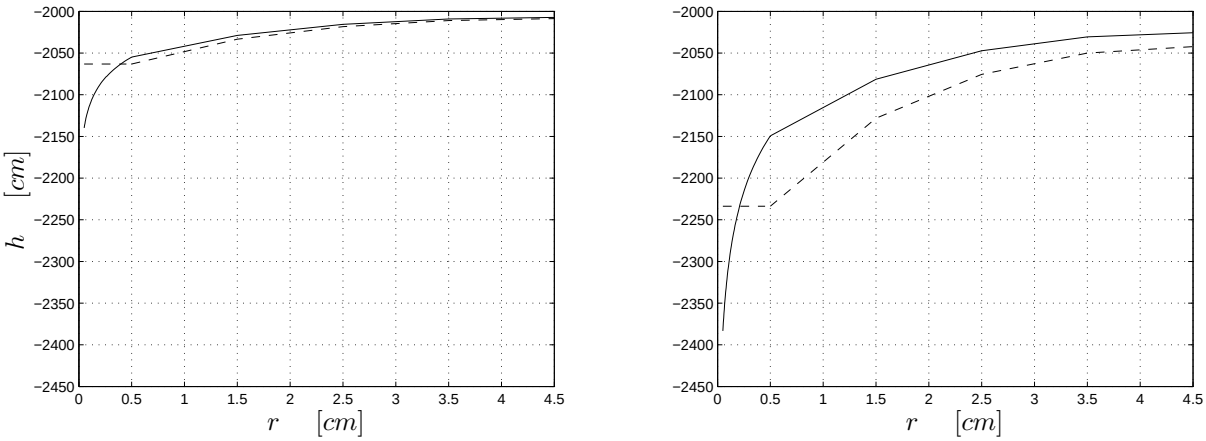


**Fig.** 2.10: Water potential distribution throughout the soil at soil layer $z = -4$ cm without hydraulic conductivity drop near the root (dashed line) and with hydraulic conductivity drop (solid line). Left: low $L_r^*$ scenario. Right: higher $L_r^*$ scenario.

drop within the soil voxel around the root segment was considered. The absolute water potential at the soil-root interface, however, was larger. As a consequence, the hydraulic gradient between the soil-root interface and the xylem was smaller and the simulated water extraction was less.

The final quantity that was assessed is the total flow at the root collar $J_c$, as illustrated

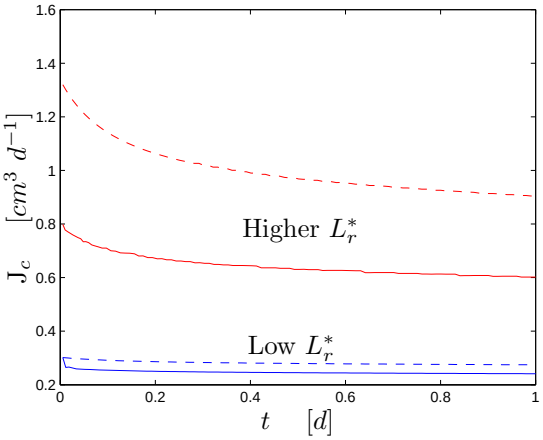


**Fig.** 2.11: Total water flow at the root collar $J_c$ as function of the simulation time without considering the hydraulic conductivity drop (dashed line) and with hydraulic conductivity drop (solid line). The low $L_r^*$ scenario is denoted by the blue lines, the higher $L_r^*$ scenario by the red lines.

in Fig. 2.11 for both scenarios with and without conductivity drop. It can be noticed that for the low radial root conductivity scenario, the average change in exponential decay of

the total water flow at the root collar considering the conductivity drop was about 14% less than in the case where the conductivity drop was not considered. This was caused by the change in radial soil-root water flow. In the higher radial root conductivity scenario, the average change in total water flow between the two methods of estimation of the water potential at the soil-root interface was about 50%. This indicates that the effect of the water potential gradient, seeming relative small in percentage, between the bulk soil and soil-root interface may have a big influence on the estimated total water flow at the root collar. Especially in those situations where radial root hydraulic conductivity is larger than soil hydraulic conductivity.

### 2.5.3 Validation scenario: mesh refinement

Accuracy for low radial root conductivity

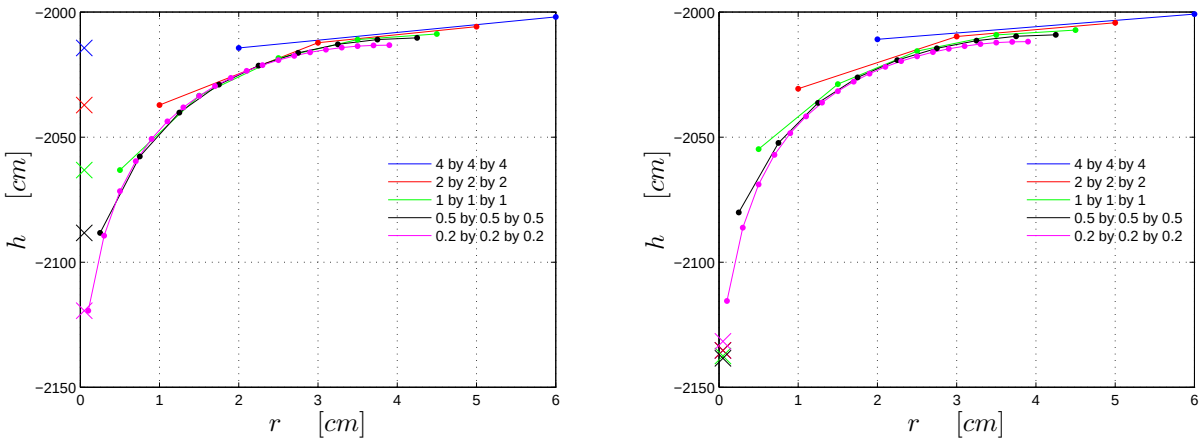


**Fig.** 2.12: Soil water potential distribution for various voxel sizes at rooting depth $z = -4$ cm without hydraulic conductivity drop around the root (left) and with hydraulic conductivity drop around the root (right). The soil-root interface water potential is denoted with 'x'. The voxel size represents the x, y and z-direction of a voxel in cm. At $r = 0$ a vertical root is positioned.

Fig. 2.12 shows that, indeed, the soil water potential distribution was affected by the element size and that the soil-root interface water potential was more precisely estimated for smaller elements.

The left graph of Fig. 2.12 shows the soil water potential distribution without considering the hydraulic conductivity drop around the root (average approach). The water potential at the soil-root interface (crosses in Fig. 2.12) is equal to the water potential in the bulk soil. If the local hydraulic conductivity drop is explicitly considered around

the root (analytical approach), we see (right graph in Fig. 2.12) that the estimated water potential at the soil-root interface is always better estimated regardlessly the grid resolution. The observed discrepancies in water potential at the soil-root interface for all grid resolutions were smaller than 1% (Table 2.3) and insignificant.

An interesting point is the gain in accuracy when taking the hydraulic conductivity drop explicitly into account as opposed to not considering the conductivity drop. Therefore, we analyzed the water potentials estimated at the soil-root interface for all grid resolutions compared to the most accurate estimated water potential, i.e. for the 0.2 by 0.2 by 0.2 cm voxel and considering the hydraulic conductivity drop. From Table 2.3 it can be deduced that if the local hydraulic conductivity drop is taken into account the soil-root interface water potential can be estimated with more accuracy for equal soil discretizations than by using the average method. Considering the average approach, the smallest element (0.2 by 0.2 by 0.2 cm) satisfies the smaller than 1% limit and predicts water potentials that are in range with the reference scenario. For increasing element size, however, the deviation increases. The discrepancies seem very small; keep in mind, though, that a homogeneous clay soil was investigated and the root was not affected by plant stress conditions. This will not lead to large simulated water potentials near the root and will have less effect on differences in both approaches. Despite the relative small changes in water potential, we observed significant overestimation in radial soil-root water flow (Table 2.3). For larger elements, a difference larger than 10% is noticeable when not considering the hydraulic conductivity drop compared with the reference scenario.

**Table** 2.3: Relative error in water potential [$h$] at the soil-root interface and in radial soil-root water flow [$J_r$] for various element sizes with respect to the element size 0.2 by 0.2 by 0.2 cm considering the hydraulic conductivity drop. Low radial root conductivity scenario at rooting depth $z = -4$ cm.

| | Element size [cm] | | | | |
|---|---|---|---|---|---|
| | 0.2 by 0.2 by 0.2 | 0.5 by 0.5 by 0.5 | 1 by 1 by 1 | 2 by 2 by 2 | 4 by 4 by 4 |
| Average [$h$] | 0.6 % | 2 % | 3.3 % | 4.4 % | 5.5 % |
| Analytical [$h$] | - | 0.3 % | 0.3 % | 0.2 % | 0.2 % |
| Average [$J_r$] | 2.2 % | 7.4 % | 10.9 % | 14 % | 16.8 % |
| Analytical [$J_r$] | - | 1.3 % | 1.3 % | 1.6 % | 3.3 % |

### Accuracy for higher radial root conductivity

We have seen above that an increase in radial root conductivity leads to a greater water uptake around the roots and affects the water potential distribution throughout the soil. If we compare the difference in water potential estimated at the soil-root interface and in ra-

dial soil-root water flow for all grid resolutions with and without considering the hydraulic conductivity drop, it can be noticed from Table 2.4 that the error has increased at least 2-fold compared with the low $L_r^*$ scenario (Table 2.3). For larger elements, the error in radial soil-root water flow when not considering the hydraulic conductivity drop is larger than 30% compared with the reference scenario.

With these validation scenarios we have shown that incorporation of the local hydraulic conductivity drop around individual roots in R-SWMS can solve problems with greater accuracy for larger grid resolutions compared with not considering the hydraulic conductivity drop.

**Table** 2.4: Relative error in water potential [$h$] at the soil-root interface and in radial soil-root water flow [$J_r$] for various element sizes with respect to the element size 0.2 by 0.2 by 0.2 cm considering the hydraulic conductivity drop. Higher radial root conductivity scenario at rooting depth $z = -4$ cm.

| | Element size [cm] | | | | |
|---|---|---|---|---|---|
| | 0.2 by 0.2 by 0.2 | 0.5 by 0.5 by 0.5 | 1 by 1 by 1 | 2 by 2 by 2 | 4 by 4 by 4 |
| Average [$h$] | 1% | 4% | 6% | 9% | 13% |
| Analytical [$h$] | - | <1 % | <1% | 2% | 4% |
| Average [$J_r$] | 6 % | 20 % | 29 % | 38 % | 44 % |
| Analytical [$J_r$] | - | 4 % | 4 % | 6 % | 7 % |

### Computational times

For a soil discretization of 0.2 by 0.2 by 0.2 cm without explicitly taking the hydraulic conductivity drop into account, the water potential at the soil-root interface approached the one estimated where the hydraulic conductivity drop was considered. The computational time, however, increased largely for such a small element, as can be seen in Table 2.5. Here, the factor of decrease in computational time of the elements using both methods are compared with the 0.2 by 0.2 by 0.2 element without considering the hydraulic conductivity drop. Not only was a greater accuracy obtained for larger grid resolutions when considering the hydraulic conductivity drop, but also a significant gain in computational speed compared with neglecting the hydraulic conductivity drop.

**Table** 2.5: Factors of decrease in computational time for various element sizes with respect to the element size 0.2 by 0.2 by 0.2 cm without considering the conductivity drop.

| | Element size [cm] | | | |
|---|---|---|---|---|
| | 0.5 by 0.5 by 0.5 | 1 by 1 by 1 | 2 by 2 by 2 | 4 by 4 by 4 |
| Average | 12 | 60 | 95 | 100 |
| Analytical | 5 | 25 | 43 | 86 |

## 2.6 Conclusions

It was shown that the hydraulic conductivity drop at the voxel scale, from bulk soil to soil-root interface, cannot always be neglected and that it can be quantified with microscopic models coupled to soil-root water transfer models.

The microscopic model has shown that the largest drop is noticed at the moment plant stress occurs. The amplitude of the conductivity drop and time occurrence of plant stress is very much dependent on soil and root properties. Furthermore, the time occurrence is affected largely, even under small conductivity drops, if the hydraulic conductivity drop is not considered and the bulk soil conductivity equals the soil-root interface conductivity.

As observed, the effect of the hydraulic conductivity drop on water uptake for single roots in the 3D soil-root water transfer model is considerable, even for relatively wet soils, especially under conditions where the radial root conductivity is larger than the soil hydraulic conductivity. These findings were reinforced by numerical validation using mesh refinement.

Furthermore, incorporation of the hydraulic conductivity drop around individual roots in a 3D soil-root water transfer model can solve problems for larger grid resolutions with still an acceptable accuracy and with smaller computational times than with the distance-based averaging procedure where the hydraulic conductivity drop is not considered.

Assessment of the accuracy of the simulated water uptake could only be based on numerical validation. New non-invasive techniques like NMR (Pohlmeier *et al.*, 2008) could allow us to assess soil-root interactions at the voxel scale and test our assumptions against real observations.

More work should be done on the effect of the hydraulic conductivity drop at the plant scale, using larger, more realistic root structures. Simulation of water flow in large root structures costs lots of computational power. Parallelization tools are needed to solve the water flow in soil (Hardelauf *et al.*, 2007) and roots.

# Chapter 3

# Implementation of a microscopic soil-root hydraulic conductivity drop function in a 3D soil-root water transfer model*

## 3.1 Objectives

In Chapter 2 an analytical microscopic approach was build and numerically validated to estimate the local soil hydraulic conductivity drop around single roots in the 3D soil-root water transfer model of Javaux *et al.* (2008). In this chapter the impact of the local hydraulic conductivity drop on denser root architectures and in dry soil regions (near plant stress) is addressed. Different geometrical applications of the microscopic model, describing the hydraulic conductivity drop for multiple roots within a soil voxel of a 3D soil-root water transfer model, are implemented. These simplifications, originating from 1D models, are assessed for two sets of soil hydraulic properties and for four simplified root architectures in different growing stages. The results of the different subvoxel simplifications of the microscopic water flow towards roots are compared to a numerical simulation that resolves the smaller scale water potential gradients by using a much finer grid.

*adapted from T. Schröder, M. Javaux, J. Vanderborght, B. Körfgen, and H. Vereecken (2009). Implementation of a microscopic soil-root hydraulic conductivity drop function in a 3D soil-root architecture water transfer model. Vadose Zone Journal, in press

## 3.2 Introduction

The understanding of spatial and temporal root water uptake is of importance for a variety of environmental and agricultural purposes, such as irrigation management and yield prediction under water scarcity conditions. It is known that water is taken up in proportion to the water potential difference between soil and root and that it is dependent on the hydraulic conductivity in the vicinity of the roots. However, there is a long ongoing debate regarding the relative magnitude of the water flow resistance due to soil and root (Newman, 1969; Taylor and Klepper, 1975; Nobel and Cui, 1992). Several authors argued that the water potential gradient in the vicinity of roots could among other things be due to bad soil-root contacts (Huck *et al.*, 1970; Tinker, 1976; Herkelrath *et al.*, 1977; Bristow *et al.*, 1984) or the fact that only a few roots could be active (Passioura, 1980). High water potential gradients, however, imply that important water potential differences exist between bulk soil and soil-root interface and that soil properties limit the potential root water uptake (Li *et al.*, 2002b; Garrigues *et al.*, 2006). The difficulty of measuring the soil water status near the soil-root interface makes the experimental verification of these hypotheses hard. Besides the experimental investigations, numerical models that explicitly consider the water potential gradient near the roots are needed to evaluate these important soil-root interactions. Different 1D models explicitly consider the soil water potential gradient for the prediction of root water uptake (Gardner, 1960; Cowan, 1965; Hillel *et al.*, 1975; De Willigen and van Noordwijk, 1987; De Jong van Lier *et al.*, 2006) applied at the single root level (microscopic scale). On the macroscopic scale, there are 1D models using extraction functions (Feddes *et al.*, 1976) but usually without consideration of the water potential gradient between bulk soil and the soil-root interface.

Developments in modelling approaches of the root architecture and of the root hydraulics have lead to the current state of the art in modelling root water uptake: fully coupled 3D soil-root models (Doussan *et al.*, 2006; Javaux *et al.*, 2008). These 3D models predict root water uptake based on water potential differences in soil and roots. Again, the crucial point in these 3D models is the resistance between bulk soil and soil-root interface. Currently, 3D models assume the bulk soil water potential to be equal to the soil-root interface water potential, neglecting the hydraulic conductivity drop within a soil voxel surrounding roots (in the model of Javaux *et al.* (2008) a soil voxel is a regular hexahedron). This may become problematic when the soil resolution is too coarse. Due to the non-linearity of the soil hydraulic conductivity, root water uptake may lead to considerable water potential gradients at the soil-root interface, which are not depicted by the numerical

grid that is used to describe the bulk soil water movement.

## 3.3 Theory

### 3.3.1 3D macroscopic water flow model in soil and roots

The model of Javaux *et al.* (2008) consists of two interacting systems: the soil matrix and the root architecture. For both systems a set of equations is solved in terms of water potential and both are coupled via the sink term $S$ in the Richards equation, see Javaux *et al.* (2008) for more details. In this study, the boundary conditions for the plant root system are a transpiration rate at the root collar, and a soil water potential at the soil-root interface enabling calculation of the water potential within the roots. Stress is defined when the water potential at the root collar is lower than a limiting water potential value. From this point on the actual transpiration rate is lower than the potential transpiration rate.

Radial soil-root water flow $J_r$ [cm$^3$ d$^{-1}$] is given by

$$J_r = L_r^* A_r (h_{int} - h_{xylem}) \tag{3.1}$$

where $L_r^*$ is the radial root conductivity [d$^{-1}$], $A_r$ [cm$^2$] the root outer surface and $h$ [cm] represents the water potential expressed as hydraulic head at the soil-root interface ($h_{int}$) and in the xylem ($h_{xylem}$) respectively. The outer root surface is defined by $A_r = 2\pi r_{int} l_r$, with $r_{int}$ [cm] the root radius from the center of the xylem to the soil-root interface and $l_r$ [cm] the length of the root segment. The radial root conductance is given by $L_r = L_r^* A_r$ [cm$^2$ d$^{-1}$]. The water potential at the soil-root interface is estimated by a distance-based weighting function of the water potential in the surrounding soil nodes. The sink term [d$^{-1}$] of a soil voxel $j$ is calculated by

$$S_j = \frac{\sum_{k=1}^{n_j} J_{r,k}}{V_j} \tag{3.2}$$

where the numerator represents the sum of all the radial soil-root fluxes of the $n_j$ root nodes located inside a soil voxel $j$ and $V_j$ [cm$^3$] is the volume of the $j^{th}$ soil voxel. A root node is defined as the center of a root segment at which water exchange is allowed. The

sink term is distributed upon the soil nodes $i$ representing the bulk soil

$$S_i = S_j \frac{\frac{(h_i - h_{int})}{dist_i}}{\sum_{k=1}^{8} \frac{(h_k - h_{int})}{dist_k}}, \qquad \text{for } i = 1, \ldots, 8 \tag{3.3}$$

where $dist$ is the distance from the soil node $i$ to the soil-root interface.

### 3.3.2 Microscopic model

A quasi 2D horizontal microscopic analytical model was previously derived by Schröder *et al.* (2008). This approach led to a good approximation of the water potentials and water fluxes close to the soil-root interface obtained using a numerical simulation for a higher spatial discretization. It should be noted, however, that we assume that the Richards equation can be used to describe water potential gradients at the subvoxel scale and that the hydraulic parameters do not vary in the vicinity of the soil-root interface. The drawback, however, is the stage at which the root cannot be considered a point in space anymore and the volume of the soil voxel is affected by the volume of the root segment. We therefore introduce a volume percentage

$$pV = \frac{\sum_{i=1}^{n} V_{seg_i}}{V_{vox}} \times 100 \tag{3.4}$$

where $V_{seg} = \pi r_{int}^2 l_r$ equals the volume of a root segment, $n$ is the number of root segments in the soil voxel and $V_{vox}$ is the volume of the soil voxel. If the volume percentage is below 5% the effect of the root segment volume on the water content in a soil voxel is still assumed to be marginal. We then assume validity of the postulation to consider the root nodes as points in this soil voxel.

The hydraulic conductivity drop in the soil between the soil nodes surrounding a root segment (bulk soil) and the soil-root interface was analytically estimated using the radial Richards equation given by

$$\frac{\partial \theta}{\partial t} = \frac{1}{r} \frac{\partial}{\partial r} (r K(h) \frac{\partial h}{\partial r}) = -\frac{q}{r} - \frac{\partial q}{\partial r} \tag{3.5}$$

where $q$ [cm d$^{-1}$] is the Darcy's flow (a flux density) denoted by $q = -K(h)\frac{\partial h}{\partial r}$, $r$ [cm] the radial coordinate and $t$ [d] the time. The volumetric water content $\theta$ [cm$^3$ cm$^{-3}$] and the hydraulic conductivity $K$ [cm d$^{-1}$] are soil characteristics, dependent on the water

potential. The differential equation is linearized using the matric flux potential

$$\Phi_h = \int_{h_{-\infty}}^{h} K(h)dh \tag{3.6}$$

where $h$ is the current water potential and $h_{-\infty}$ the lower integral boundary representing the permanent wilting point. Finally, for flux boundary conditions at the soil-root interface ($r_{int}$), imposed water potential and flux boundary conditions at the bulk soil ($r_{bulk}$), and assuming steady rate behavior, i.e. $\frac{\partial\theta}{\partial t}$ = constant, Eq. (3.5) results in

$$\Phi(r) = \Phi_{r_{bulk}} + (q_{int}r_{int} - q_{bulk}r_{bulk}) \left( \frac{{}^{r^2}/_{r_{int}^2}}{2(1-\rho^2)} + \frac{\rho^2}{1-\rho^2} \left( \ln\frac{r_{bulk}}{r} - \frac{1}{2} \right) \right) +$$

$$+ \; q_{bulk}r_{bulk}\ln\frac{r}{r_{bulk}} \tag{3.7}$$

with $\rho = {}^{r_{bulk}}/_{r_{int}}$. The water potential is derived from $\Phi(r)$ using Eq. (3.6). The steady rate behavior is shown to be a valid assumption (De Willigen and van Noordwijk, 1987; De Jong van Lier *et al.*, 2006; Schröder *et al.*, 2008). Schröder *et al.* (2008) showed that the error induced by the steady rate assumption, compared to numerical simulations, is small and below 5% in very dry sandy soils. To keep the error within the 3D model small, especially when larger changes in soil water content are noticed, the timestep should be controlled and decreased. An additional criterion was implemented in the 3D model that ensures that changes in the radial soil-root flow of a root segment, between the previous and current solution, are small. If this condition is not fulfilled and a maximum number of iterations is reached the model reduces the timestep and restarts the current simulation time.

### 3.3.3 Water potential criterion at the soil-root interface

From the derived conductivity drop from bulk soil to soil-root interface and the flow from soil-root interface to the root xylem vessel a criterion can be derived for the water potential at the soil-root interface, relating the local average soil hydraulic conductivity to the radial root conductivity.

From Eq. (3.7) we can obtain the flux of water at the soil-root interface ($q_{int}$), using Eq. (3.6),

$$q_{int} = \frac{\bar{k}B}{r_{int}} \left( h_{bulk} - h_{int} \right) + B\chi_1 + \chi_2 \tag{3.8}$$

where

$$\bar{k} = \frac{\int_{h_{int}}^{h_{bulk}} K(h)dh}{h_{bulk} - h_{int}} = \frac{\Phi_{r_{bulk}} - \Phi_{r_{int}}}{(h_{bulk} - h_{int})} \geq 0$$

$$B = \frac{2(1-\rho^2)}{-2\rho^2(\ln\rho - 1/2) - 1}, \quad B > 0 \quad \text{for} \quad \rho > 1 \tag{3.9}$$

$$\chi_1 = q_{bulk}\ \rho\ \ln 1/\rho \quad \text{and} \quad \chi_2 = q_{bulk}\ \rho$$

Because of conservation, the water flux arriving at the soil-root interface (Eq. (3.8)) equals the water flux from soil-root interface to the xylem; $q_{int} = {}^{J_r}/_{A_r} = L_r^*(h_{int} - h_{xylem})$ (derived from Eq. (3.1)). Extraction of the soil-root interface water potential yields

$$h_{int} = \frac{\bar{k}Bh_{bulk} + L_r^* r_{int} h_{xylem} + Br_{int}\chi_1 + r_{int}\chi_2}{\bar{k}B + L_r^* r_{int}} \tag{3.10}$$

Note that Eq. (3.10) is not explicit as $\overline{k}$ is dependent on $h_{int}$ (Eq. (3.9)). An asymptotic analysis of the ratio of the soil and root conductivities reveals that

$$\bar{k}B \gg L_r^* r_{int} \rightarrow h_{int} = h_{bulk} + \frac{r_{int}}{\bar{k}}\chi_1 + \frac{r_{int}}{\bar{k}B}\chi_2 \rightarrow h_{int} = h_{bulk} \tag{3.11}$$

$$\bar{k}B = L_r^* r_{int} \ \rightarrow h_{int} = \frac{1}{2}h_{bulk} + \frac{1}{2}h_{xylem} + \frac{B}{2L_r^*}\chi_1 + \frac{1}{2L_r^*}\chi_2 \tag{3.12}$$

$$L_r^* r_{int} \gg \bar{k}B \rightarrow h_{int} = h_{xylem} + \frac{B}{L_r^*}\chi_1 + \frac{1}{L_r^*}\chi_2 \tag{3.13}$$

where $L_r^* r_{int}$ is the radial root conductivity along its resistive pathway (cortex). In soil locations where $\bar{k}B \gg L_r^* r_{int}$ and the soil water potential gradient is small, the root is the limiting system. This implies that the water potentials in the root system control the water flux from soil to root. If $L_r^*$ is constant and uniform it is expected that under such conditions the sink term distribution follows the root length density trend (Coelho and Or, 1999; Li *et al.*, 2002a,b), as long as the xylem conductivity is high enough and the xylem potential does not vary considerably in the root system. Beyond the point $\bar{k}B = L_r^* r_{int}$ the soil is the limiting system. Here the water potential gradients in the soil control the flow towards the root system. A simple macroscopic relation between root water uptake and root length density is not expected as shown by Li *et al.* (2002a,b) who investigated root extraction patterns for corn at the field scale. We call this point soil limiting conditions. Effects of local soil-root interactions will be visible beyond the point

of limiting soil conditions (Eq. (3.13)) and therefore our simulations are mainly assessed in this state.

### 3.3.4 Estimation of the soil-root interface water potential for multiple roots in a 3D soil-root water transfer model

Two main approaches can be considered. In the averaging approach, as proposed by Javaux *et al.* (2008), the soil water potential distribution below the voxel scale is not explicitly taken into account and the potential at the soil-root interface is equal to the bulk soil water potential. This approach may be used when the spatial discretisation is fine enough to reproduce the soil water potential gradient towards single roots. On the other hand, if the grid discretization is too coarse to reproduce the water potential gradient at the soil-root interface, the flow towards the root for a given xylem pressure may be affected by this approach (Schröder *et al.*, 2008). In a second approach the microscopic analytical model described above can be applied at the subvoxel scale. Fig. 3.1 shows four methods. Method A represents the averaging procedure, while methods B, C and D use the analytical approach at the subvoxel scale. Methods B, C, and D differ in the definition of the outer radius of influence for the root, and in the boundary conditions. The root inner radius from xylem to soil-root interface is known for each root segment. We assume, for all methods, that the roots may be projected as points in space connected by line segments, i.e. root volume << soil voxel volume.

Method B keeps the original geometry of distribution and calculates the water potential at the soil-root interface for each individual root node. Each individual root node has an outer radius ($r_{bulk}$) that corresponds to the minimal distance between the root location and one of the soil voxel edges. Furthermore, it has a different bulk soil water potential and flux boundary condition at the outer edge. Water is extracted by each root node independently from water uptake by neighboring root nodes. This means that for each root node a bigger water reservoir is available causing probably a slight underprediction of the pressure head gradient, compared to considering the root extraction of a neighboring root node.

In scenario C the root nodes are equally redistributed and a soil voxel is subdivided in a number of small subvoxels equal to the number of root nodes in the soil voxel. The outer radius of the cylinder around the root node is kept uniform and is related to the square root of the voxel size scaled to the number of root nodes. The outer edge water potential for each root node is obtained by averaging of the soil water potentials at the corner nodes of the 2D plane (Fig. 3.1). We assume furthermore a zero flux condition that implies that

no water is extracted from the outer radius (De Willigen and van Noordwijk, 1987). This may be true regarding water extraction among neighboring root nodes within a soil voxel. It may be a large simplification when the flow towards the voxel is important compared to the water uptake by the roots. This may occur when in neighboring soil voxels a dissimilar amount of water is extracted. However, one dimensional plant uptake models often use that implicit assumption when modelling root water uptake (see e.g. De Jong van Lier *et al.*, 2007).

Method D relocates all root nodes to the middle of the soil voxel. One large root node is created for which the outer radius is equal to half the voxel size. This approach is analog to assumptions imposed by several 1D microscopic models. The flux and water potential boundary conditions at the outer edge are obtained by averaging, similar to method C. The total water that flows into the root is the sum of all the radial soil-root fluxes of the individual root nodes. As a consequence, the newly defined root radius (to be used in Eq. (3.7)) is the sum of all the root radii in the soil voxel. For estimation of the water potential gradient from the outer edge (bulk soil) to the soil-root interface the summation of the root radii may not exceed the outer defined (bulk soil) radius. After solving the analytical approach, the water potential at the soil-root interface is then given to each individual root node.

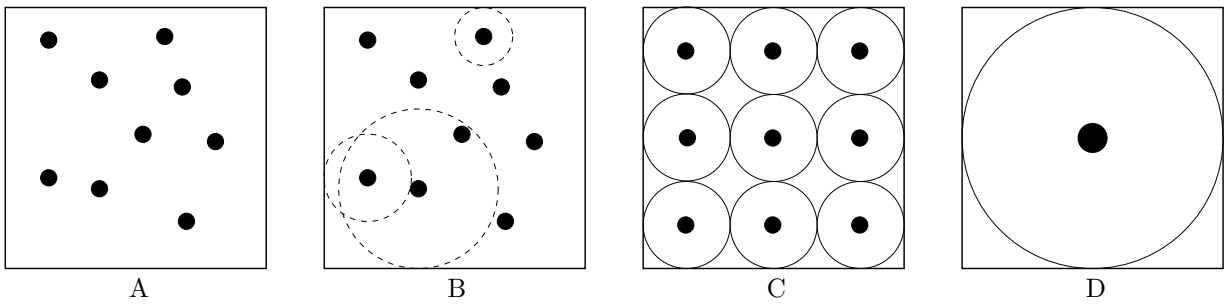


**Fig.** 3.1: Four methods for estimation of the soil-root interface water potential for the multiple root problem (2D representation). Method A represents the average approach and does not consider the local soil hydraulic conductivity drop around roots. Scenarios B, C and D incorporate the analytical approach and take the hydraulic conductivity drop explicitly into account. The black dots represent root nodes which have a radius $r_{int}$. The outer radius representing the bulk soil $r_{bulk}$ is denoted by the circles.

## 3.4 Methods

To test the proposed local root water uptake methods several well-defined scenarios have to be chosen. These scenarios need the definition of different root and soil properties

and boundary conditions for the soil and root system. We investigate four kind of root

**Table** 3.1: Frequency of number of root nodes per soil voxel for root architecture 1-4 assessed for two soil discretizations, 0.2 by 0.2 by 0.2 cm and 1 by 1 by 1 cm respectively.

| | Root architecture | Discretization [cm] | Number of root nodes in a soil voxel 1 | 2 | 3 | 4 | 5 | 6 | 7 | 8 | 9 | 10 | 11 | 12 |
|---|---|---|---|---|---|---|---|---|---|---|---|---|---|---|
| Frequency | 1 | 1 by 1 by 1 | 12 | 7 | 7 | 4 | 2 | 1 | | | | | | |
| | | 0.2 by 0.2 by 0.2 | 64 | 10 | | 1 | | | | | | 1 | | |
| | 2 | 1 by 1 by 1 | 10 | 8 | 6 | 5 | 1 | 1 | | | | | | |
| | | 0.2 by 0.2 by 0.2 | 54 | 15 | 4 | 2 | | | | | 1 | | | |
| | 3 | 1 by 1 by 1 | 14 | 19 | 11 | 9 | 8 | 6 | 7 | 1 | 5 | 3 | 2 | |
| | | 0.2 by 0.2 by 0.2 | 235 | 60 | 17 | 3 | | 1 | | | 1 | | | |
| | 4 | 1 by 1 by 1 | 25 | 28 | 15 | 17 | 7 | 7 | 11 | 3 | 3 | 8 | 7 | 1 |
| | | 0.2 by 0.2 by 0.2 | 450 | 91 | 29 | 11 | 3 | 1 | | | 1 | | | |

| | Root architecture | Discretization [cm] | Number of root nodes in a soil voxel 13 | 14 | 16 | 17 | 19 | 21 | 25 | 26 | 29 | 32 | 43 |
|---|---|---|---|---|---|---|---|---|---|---|---|---|---|
| Frequency | 1 | 1 by 1 by 1 | | | | | 1 | | | | | | |
| | | 0.2 by 0.2 by 0.2 | | | | | | | | | | | |
| | 2 | 1 by 1 by 1 | | | | 1 | | 1 | | | | | |
| | | 0.2 by 0.2 by 0.2 | | | | | | | | | | | |
| | 3 | 1 by 1 by 1 | 1 | 1 | | | | | | 1 | 1 | | |
| | | 0.2 by 0.2 by 0.2 | | | | | | | | | | | |
| | 4 | 1 by 1 by 1 | | 2 | 1 | | 1 | | 1 | | 1 | 2 | 1 |
| | | 0.2 by 0.2 by 0.2 | | | | | | | | | | | |

architectures. Each root architecture differs in the number of root nodes that are located in a soil voxel, thus in root surface density per voxel. The root architectures are generated with the root growth model from Somma *et al.* (1998). Root branches grow under different angles and root radii vary dependent on branching hierarchy. Root architecture 1 consists of primary roots only and has an average root length density $\overline{RLD}$ of 0.06 cm cm$^{-3}$. Root architecture 2 and 3 have secondary roots as well with a $\overline{RLD}$ of 0.09 and 0.24 cm cm$^{-3}$ respectively. Root architecture 4, in addition, has tertiary roots which increases the total root surface determining water uptake considerably. The calculated average root length density is 0.36 cm cm$^{-3}$. These root length densities are rather small, however, root architectures for faba beans with a RLD of order of 0.1 cm cm$^{-3}$ where found by Kage and Ehlers *et al.* (1996) in the field. Furthermore, for computational reasons we will not consider extremely large root architectures in this study. A more thorough overview of the number of root nodes per soil voxel, dependent on soil discretization, is given in Table 3.1. For simplicity, the radial root conductivity $L_r^*$, regulating root water uptake, and the axial

conductance $K_h$ [cm$^3$ d$^{-1}$], regulating axial flow in the root xylem, for the different root architectures are chosen constant and uniform, see Table 3.2. Note that the objective of this study is to investigate the effect of small scale water potential gradients and the way they are implemented in numerical models for simulating root water uptake. Therefore a non-uniform root conductivity distribution, as proposed by Doussan *et al.* (1998a), to perform realistic simulations is not considered here. However, variable root conductivities as function of time and space can easily be implemented in the model.

The soil properties are obtained via the Mualem-van Genuchten parameterization (Van Genuchten, 1980)

$$\begin{aligned} \Theta &= \left[\frac{1}{1+(\alpha h)^n}\right]^m = \frac{\theta-\theta_r}{\theta_s-\theta_r} \\ K(\Theta) &= K_s\Theta^\lambda[1-(1-\Theta^{1/m})^m]^2 \\ m &= 1-\frac{1}{n} \end{aligned} \tag{3.14}$$

where $\Theta$ is the soil saturation degree and $\theta_r$ and $\theta_s$ indicate residual and saturated volumetric water content. The saturated soil hydraulic conductivity is denoted by $K_s$, and $\alpha$, $\lambda$ and $n$ are soil parameters. Soil hydraulic parameters are given in Table 3.3. The parameters for the clay and loamy soil are based on the parameters proposed by Carsel and Parrish (1988). The soil properties are considered homogeneous.

Only water flow is simulated, no further root growth and no solute uptake is considered in the simulation. A soil column is defined with dimensions 7 by 7 by 12 cm and discretized in voxels of respectively 0.2 by 0.2 by 0.2 cm (fine discretization) and 1 by 1 by 1 cm (coarse discretization). The minimal dimension of 0.2 cm for a soil cube is chosen to ensure the existence of a representative elementary volume to apply the Richards equation. For the coarser soil discretization the average volume percentage of roots in a soil voxel, calculated by Eq. (3.4), for root architecture 4 (maximum root density) is $1.4{\cdot}10^{-3}$%. The maximum volume percentage is 5.7% near the root collar. Besides this maximal value, that is still near the imposed criterion, the average value is much lower than the criterion imposed and allows the use of the microscopic approach at this coarser soil discretization. The size of the soil column is rather small, however, for the objectives in this study and for computational reasons it is large enough to test the microscopic approaches. At the top and bottom of the soil domain (and the lateral sides) zero flux conditions are imposed. The initial soil water potential equals -1 cm throughout the soil column.

For each root architecture, simulations are performed with a specific imposed flux at the root collar. A flux boundary condition is imposed such that the whole pF spectrum can be assessed if simulations are performed over a long simulation time. Root architecture 4 is the most detailed/complex root system and is taken as point of departure. If we assume a transpiration rate of 0.3 cm $d^{-1}$ we obtain a root collar flux of 14.7 $cm^3$ $d^{-1}$ (transpiration rate times soil surface area). An average flux density per root segment can be defined by dividing the root collar flux by the total root area (Table 3.2). This value, equal to 0.2 cm $d^{-1}$, is used to calculate the root collar fluxes for the simulations performed with the other root architectures. This to ensure that the average water uptake per root segment is equal among scenarios. Root water fluxes of same order of magnitude were observed in Doussan *et al.* (1998b). A summary of the boundary conditions and properties of the root and soil is given in Table 3.2. Simulations are stopped when plant stress is reached, which is set to a xylem water potential of -15000 cm at the root collar. As can be seen from Table 3.1, for a fine soil discretization (0.2 by 0.2 by 0.2 cm), many soil voxels have one or very few root nodes. We will evaluate method A, denoted by $A_0$, as a reference method for the fine soil discretization. For the coarser soil discretization (1 by 1 by 1 cm) all four methods of microscopic treatment will be considered: $A_1$, $B_1$, $C_1$ and $D_1$ (Table 3.4).

**Table** 3.2: Root properties and boundary conditions (BC) for the four root architectures.

| Root architecture | Root properties | | Total root area [$cm^2$] | BC soil [cm $d^{-1}$] | BC root collar [$cm^3$ $d^{-1}$] |
|---|---|---|---|---|---|
| | $L_r^*$ [$d^{-1}$] | $K_h$ [$cm^3$ $d^{-1}$] | | | |
| 1 | $6.48{\cdot}10^{-5}$ | 4.32 | 15.21 | zero flux top/bottom | 3.045 |
| 2 | $6.48{\cdot}10^{-5}$ | 4.32 | 22.34 | zero flux top/bottom | 4.473 |
| 3 | $6.48{\cdot}10^{-5}$ | 4.32 | 50.15 | zero flux top/bottom | 10.038 |
| 4 | $6.48{\cdot}10^{-5}$ | 4.32 | 73.43 | zero flux top/bottom | 14.700 |

**Table** 3.3: Mualem-van Genuchten parameters for a clay and loamy soil (Carsel and Parrish, 1988).

| Textural Class | $\theta_r$ ($cm^3$ $cm^{-3}$) | $\theta_s$ ($cm^3$ $cm^{-3}$) | $K_s$ (cm $d^{-1}$) | $\alpha$ ($cm^{-1}$) | $\lambda$ | n |
|---|---|---|---|---|---|---|
| Clay | 0.1 | 0.4 | 10 | 0.01 | 0.5 | 1.1 |
| Loam | 0.08 | 0.43 | 50 | 0.04 | 0.5 | 1.6 |

**Table** 3.4: The simulated root water uptake scenarios.

| Scenario | Soil discretization [cm] | Method |
|---|---|---|
| $A_0$ | 0.2 by 0.2 by 0.2 | Averaging method |
| $A_1$ | 1 by 1 by 1 | Averaging method |
| $B_1$ | 1 by 1 by 1 | Original analytical approach |
| $C_1$ | 1 by 1 by 1 | Equidistant analytical approach |
| $D_1$ | 1 by 1 by 1 | One root analytical approach |

## 3.5 Results

### Average sink term distribution

After initialization of the simulations root water uptake will cause the soil to dry out. Following Eq. (3.11) we first expect that the water potential gradient between xylem and soil-root interface controls the distribution of the soil-root water fluxes and that the RLD profile overlaps the sink term profiles. If the soil is locally so dry that the soil hydraulic conductivity is lower than the root conductivity over its resistive pathway the soil will be the limiting factor for that location (Eq. (3.13)). The plant will therefore take the water up in other locations, where the water is more easily available. As a result local limiting root nodes affect the root water uptake pattern, explaining the basic so-called 'compensation mechanism' (Green and Clothier, 1995). Eventually, the xylem water potential at the root collar reaches plant stress conditions. These arguments correspond to the results in Fig. 3.2. Here the average sink term over depth is given for root architecture 4. We evaluate the different local root water uptake methods of Table 3.4 ($A_0$; $A_1$, $B_1$, $C_1$ and $D_1$) for the given soil textures in Table 3.3 at four simulation times. Note that for method $D_1$ stress conditions are already reached between the first and second simulation time. Moreover, method $A_0$ has reached plant stress conditions between simulation time three and four (see also Table 3.5).

Regarding the implementation of the local root water uptake methods, in general, no large discrepancies for the average sink term pattern among the local methods and between different soil discretizations are observed. To understand why there is little change in the average sink term patterns we have to evaluate the root system. The root system is modelled such that the sum of the radial root fluxes equal the imposed root collar flux. If a flux boundary condition is imposed a change in soil water potential (by e.g. a finer discretization, or considering the subvoxel conductivity drop) is followed by a change in xylem water potential (to fulfill mass conservation); no dramatic changes in radial and

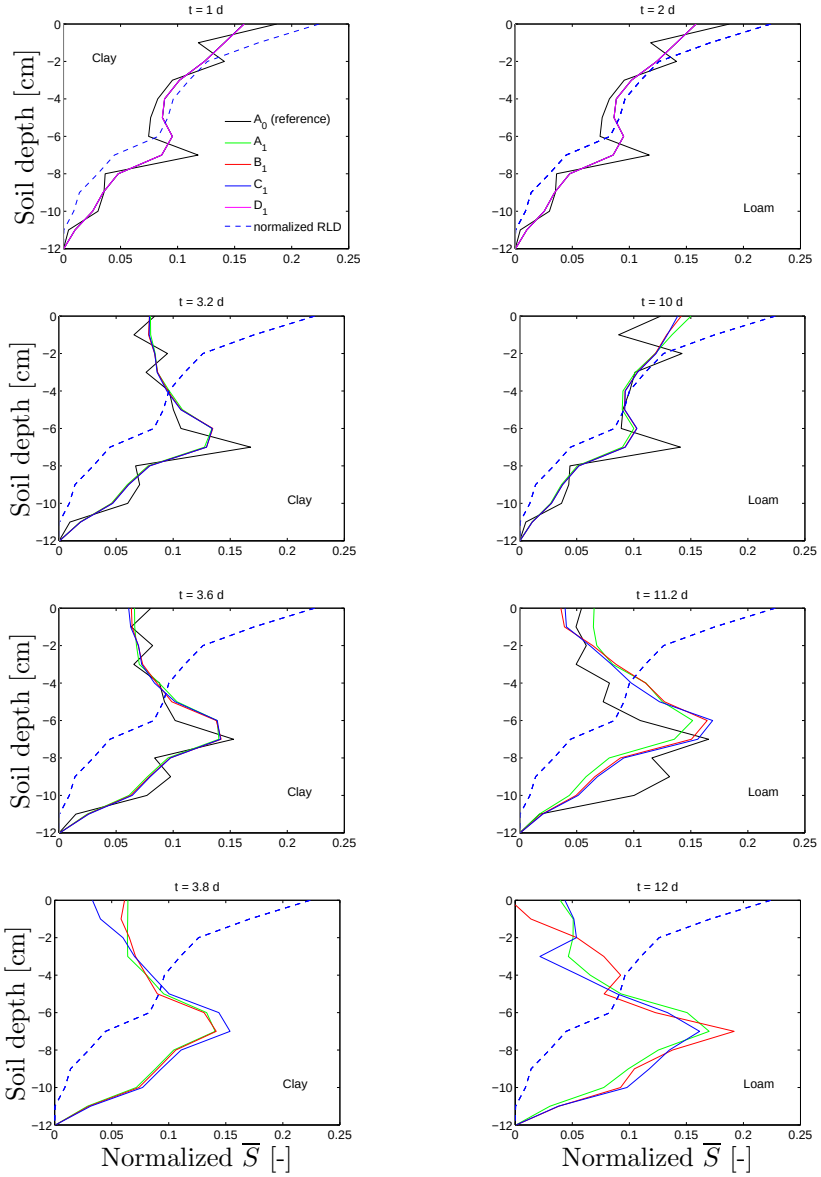


**Fig.** 3.2: Normalized average sink term against soil depth for root architecture 4 at four simulation times. The figures in the left column represent the clay soil, the figures in the right column the loamy soil. Two different conditions are evaluated. The top figures present no limiting soil conditions (Eq. (3.11)). In the other figures several root nodes are under soil limiting conditions (Eq. (3.12) and Eq. (3.13)). The different local root water uptake methods are indicated with the colored lines: $A_0$ (black) (fine discretization); $A_1$ (green), $B_1$ (red), $C_1$ (blue) and $D_1$ (magenta) (coarse discretization). The dashed line represents the normalized root length density profile.

axial root fluxes occur. Fig. 3.2 shows small discrepancies at simulation time 11.2 and 12 d for the loamy soil. For simulation time 11.2 d the soil is already much dryer considering the fine discretization, indicating a larger soil resistance near roots which leads to smaller radial soil-root fluxes. After maximal uptake, compensation mechanisms cause root nodes

in wetter soil regions to extract more water. Besides these local changes in magnitude of the radial soil-root fluxes (or sink term) the water extraction pattern stays more or less similar.

### 3.5.1 Effect of root water uptake methods at the microscopic scale

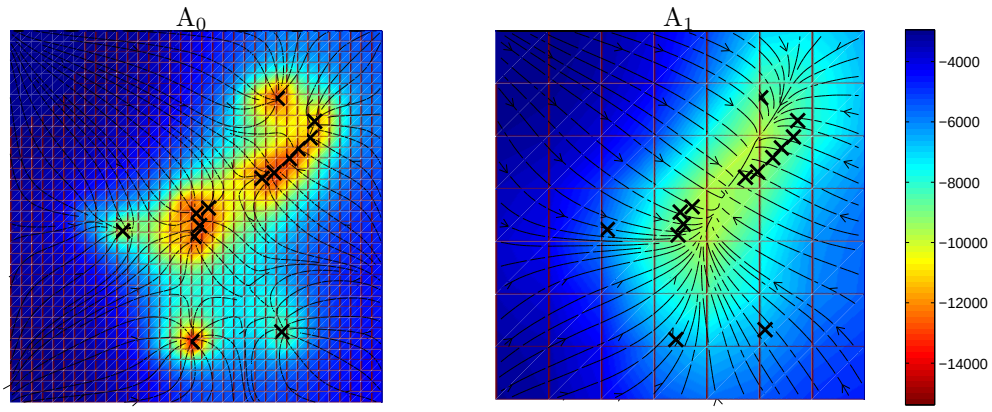


**Fig.** 3.3: A x-y cross-section at z = -2 cm shows the soil water potential [cm] distribution (color coded) and velocity profiles (black lines) at simulation day 3.6 for root architecture 4 in a clay soil. The left panel depicts root water uptake method $A_0$ (fine discretization) and the right panel method $A_1$ (coarse discretization). The black crosses represent root nodes located in this cross-sectional plane.

First we evaluate the effect of a finer and coarser soil discretization on the water potential and velocity distribution in the soil. A cross-section of the soil column for method $A_0$ (fine discretization) and method $A_1$ (coarser discretization) is shown in Fig. 3.3. In the simulations with the fine soil discretization the water flow is better resolved towards the individual root nodes. Furthermore, the water potential near the root is considerably lower than in the scenario with a coarser spatial grid. In principle, the lateral water potential distribution is affected. It is important to consider a fine soil discretization to estimate proper water potentials and velocity profiles near the root.

When the soil starts being the limiting factor at certain locations the choice of the local root water uptake methods will affect the water potential at the soil-root interface and in the xylem. As a consequence the soil water potential distribution, water flux streamlines and soil water content distribution will change. Depth profiles of the averaged soil water potential, water content, soil-root interface water potential and xylem water potential are given in Figs. 3.4 and 3.5 for root architecture 4 in a clay soil. Method $D_1$ has already reached stress conditions and is therefore not depicted in these figures. Figs. 3.4 and

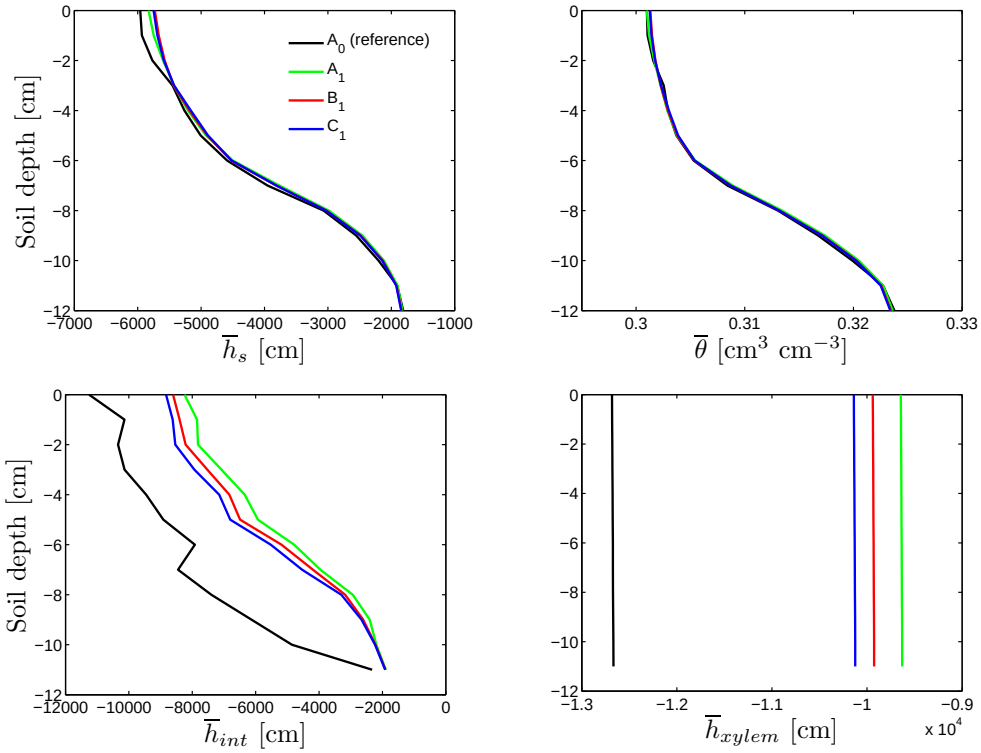


**Fig.** 3.4: The averaged soil water potential (top left), soil water content (top right), soil-root interface water potential (bottom left) and water potential in the root xylem (bottom right) are plotted as function of soil depth for root architecture 4 using a *clay soil* at $t = 3.6$ *d*. The different local root water uptake methods are indicated with the colored lines: method $A_0$ (black) (fine discretization); $A_1$ (green), $B_1$ (red) and $C_1$ (blue) (coarse discretization).

3.5 present two different simulations times (near plant stress). At the first time (Fig. 3.4) the simulation using the fine soil discretization nearly reached stress conditions. At the second time (Fig. 3.5) the simulation using the fine soil discretization has already reached stress conditions, while simulations using the coarser soil discretization, including the local conductivity drop, have almost but not reached this point. Although the soil-root interface and xylem water potentials differ a lot among methods (Fig. 3.4, bottom), the bulk soil water potential distributions and corresponding water content profiles are quite similar. A difference for soil water potential can be noticed, mainly discriminating coarse and fine soil discretizations. If we analyze the average water potential at the soil-root interface and in the xylem over depth for the coarse soil discretization, water potentials are lower for the methods that take the local hydraulic conductivity drop into account ($B_1$, $C_1$) compared to method $A_1$ neglecting the local conductivity drop. In the upper soil layers relative differences in soil-root interface water potential, between considering the local conductivity

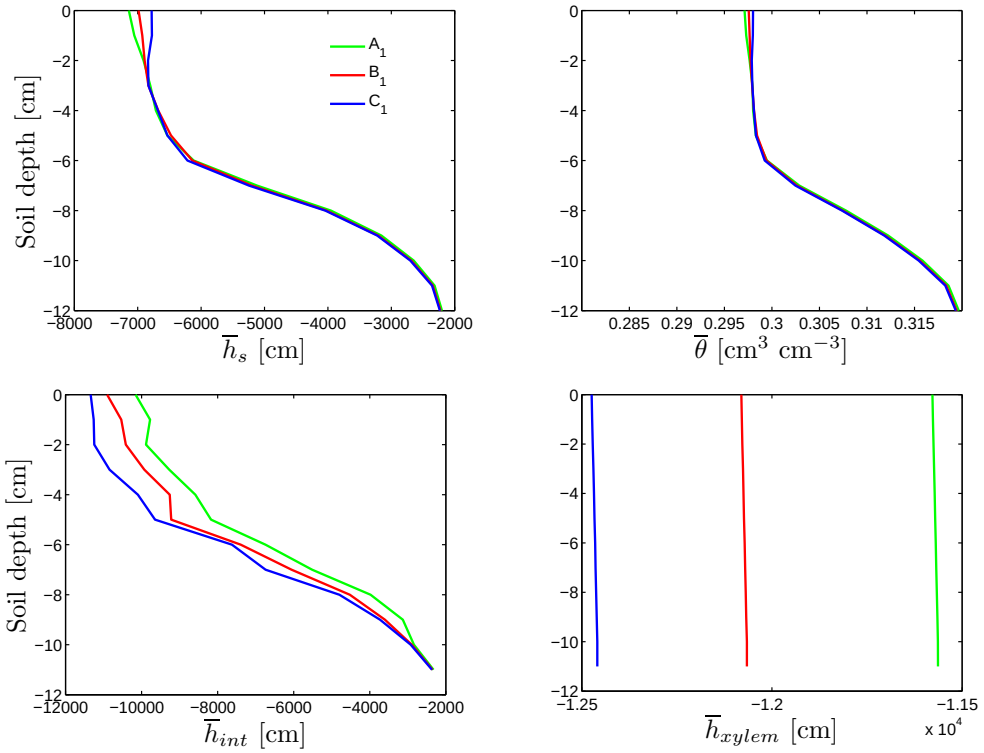


**Fig.** 3.5: The averaged soil water potential (top left), soil water content (top right), soil-root interface water potential (bottom left) and water potential in the root xylem (bottom right) are plotted as function of soil depth for root architecture 4 using a *clay soil* at $t = 3.8$ *d*. The different local root water uptake methods are indicated with the colored lines: $A_1$ (green), $B_1$ (red) and $C_1$ (blue) (coarse discretization).

drop and neglecting the local conductivity drop, of about 5% (between method $B_1$ and $A_1$) and 10% (between method $C_1$ and $A_1$) are observed. For the xylem water potential these differences are approximately 3% and 5%. If we evaluate these quantities at a later simulation time (Fig. 3.5) the water potential difference is increased by a factor of 1.7 for both the soil-root interface and xylem water potential.

Same trends are found for results of the loamy soil (not shown), however, larger changes are observed caused by the soil properties. For the loamy soil relative differences in soil-root interface water potential, between considering and not considering the local conductivity drop, of about 24% (between method $B_1$ and $A_1$) and 29% (between method $C_1$ and $A_1$) are observed. For the xylem water potential this change is approximately 21% for both methods $B_1$ and $C_1$ compared to method $A_1$.

If the local hydraulic conductivity drop is considered lower soil-root interface and xylem water potentials are obtained. This implies that plant stress conditions at the root collar will be reached earlier (Table 3.5). The time at which the stress condition is reached is an

indicator of the integrated local soil-root interactions at the root system scale. Table 3.5 shows that there is an increase in the time occurrence of stress, for a loamy soil over a clay soil, between method $A_1$ (without conductivity drop) and methods $B_1$, $C_1$ and $D_1$ (with conductivity drop). Furthermore, the imposed transpiration at the root collar has a large effect on the estimated time at which stress conditions occur. Analyzing the local root water uptake methods at the coarser soil discretization shows us that plant stress is reached earlier considering the local conductivity drop (methods B and C) as not considering the conductivity drop (method A). This is conform with the observations in Figs. 3.4-3.5. However, method D is not conform these observations. In low RLD architectures plant stress is reached later, implying that the conductivity drop considered with the one root approach is underestimated. Whereas in higher RLD architectures, the conductivity drop is overestimated and plant stress is reached much earlier than considering the fine soil discretization.

**Table** 3.5: The time occurrence of plant stress ($t_s$) for all five root water uptake methods ($A_0$; $A_1$, $B_1$, $C_1$ and $D_1$) evaluating the four root architectures for the clay and loamy soil of Table 3.3.

| Root architecture | | | Clay | | | | |
|---|---|---|---|---|---|---|---|
| | | | $A_0$ | $A_1$ | $B_1$ | $C_1$ | $D_1$ |
| 1 | $t_s$ | [d] | 16.0 | 17.4 | 16.9 | 16.4 | 17.9 |
| 2 | $t_s$ | [d] | 10.5 | 11.5 | 11.2 | 11.0 | 11.4 |
| 3 | $t_s$ | [d] | 5.0 | 5.5 | 5.4 | 5.3 | 5.0 |
| 4 | $t_s$ | [d] | 3.7 | 4.0 | 4.0 | 3.9 | 2.1 |

| Root architecture | | | Loam | | | | |
|---|---|---|---|---|---|---|---|
| | | | $A_0$ | $A_1$ | $B_1$ | $C_1$ | $D_1$ |
| 1 | $t_s$ | [d] | 50.9 | 55.5 | 53.3 | 52.4 | 57.8 |
| 2 | $t_s$ | [d] | 34.4 | 37.4 | 36.4 | 35.9 | 38.1 |
| 3 | $t_s$ | [d] | 16.0 | 17.6 | 17.0 | 16.7 | 16.9 |
| 4 | $t_s$ | [d] | 11.3 | 12.5 | 12.2 | 12.2 | 8.7 |

### 3.5.2 Mass balance

The equations used for the soil and root system approximate the water potentials and fluxes. The total system must be mass conservative. Incorporation of the local methods affect the mass balance error. In general, averaged mass balance errors are low (below 1%) and increase slightly under limiting soil conditions. Large mass balance errors are observed for method $D_1$ for root architecture three and four for a clay and loamy soil. This coincides

with the results from Table 3.5. For root architecture four (clay soil) methods $A_1$, $B_1$ and $C_1$ show larger mass balance errors as well (between 1 and 2%). These are induced by the large transpiration and the low soil water capacity, but are still considered marginal.

## 3.6 Discussion

If we compare, for flux boundary conditions at the root collar, the sink term distribution (Fig. 3.2) for methods A, B, C and D at a coarse spatial resolution with method A at the fine soil discretization, it is difficult to discriminate which root water uptake method is the most appropriate to use. Few discrepancies in root water uptake profiles are noticeable. From a modelling point of view the invariance of the water uptake profiles to local soil-root interactions, however, may be of high interest for upscaling procedures. On the other hand, at the coarser soil discretization, accounting for the local hydraulic conductivity drop, significantly lower water potentials at the soil-root interface and, consequently, in the xylem are calculated, causing stress conditions (measure for local soil-root interactions) to be reached earlier, compared to neglecting the local conductivity drop. However, none of the local methods at a coarse soil resolution can obtain the accurate results at the fine soil resolution where the soil water potential gradient is estimated steeper, resulting in lower calculated soil-root interface and xylem water potentials and consequently in the earlier occurrence of stress. The steeper soil gradient is acquired due to the more accurate spatial interpolation (Schröder *et al.*, 2008).

For higher density root architectures method C seems to be the best estimator of root water uptake among the evaluated procedures at a coarser soil discretization. With this method stress is reached earlier than with all other local methods. Probably due to the dry conditions, it is likely that neighboring root nodes within a soil voxel will not exchange much water and the zero flux condition predicts a better local drop than method B where neighboring effects are neglected. Method D seems to fail for all simulations. The underestimation of the hydraulic conductivity drop for low RLD architectures using method D can be explained with the following example. Assume that for low RLD architectures a soil voxel is occupied by one root segment. For method D this segment is centered in the soil voxel and the outer radius over which the drop occurs (from bulk soil to soil-root interface) is mostly larger than the original outer radius of this root segment. This means the drop is estimated less steep then it would do originally. In opposite case of higher RLD architectures the problem lies in the accumulation of the radial soil-root fluxes at the inner boundary of the centered root segment. The soil voxel can not sustain such a high

demand.

Note that the simulations were performed under flux boundary conditions at the root collar. If water potential boundary conditions are imposed it is expected that the xylem water potentials will not deviate largely among the local uptake methods. Estimated soil-root interface water potentials then define the magnitude of the sink term. If the local conductivity drop is neglected, higher water potentials are obtained at the soil-root interface compared to considering the conductivity drop. As a consequence larger sink terms are estimated and the soil will dry quicker. Under water potential boundary conditions root water uptake profiles are expected to differ largely for the evaluated methods.

## 3.7 Conclusions

Incorporation of microscopic effects in macroscopic models to estimate the water potential near roots in 3D soil-root models is shown to have an effect on predicted root water uptake. Which local root water uptake method gives the best description of root water uptake depends largely on soil and root properties. After comparison of the local root water uptake methods at a coarse soil discretization, for denser root architectures, the equidistant approach (method C) seems to forecast root water uptake the best. Furthermore, the 1D assumption proposed in method D does not lead to correct 3D results. The water potential compensation introduced by calculating the local conductivity drop around roots for a coarser soil grid resolution does not compute similar results as obtained with a fine soil resolution. The effect of linear interpolation in and between soil elements of the finite element method on the water potential estimation is bigger than locally implementing the water potential gradient. A fine soil resolution is therefore needed. The computational costs of a fine resolution grid are large for complicated 3D soil-root models. Therefore numerical improvements such as quickly resolving regular (fine) soil grids, or the use of irregular soil grids (Wilderotter, 2003) are needed.

At a coarse soil discretization and for limiting soil conditions, i.e. at locations where the soil hydraulic conductivity is lower than the radial root conductivity along its resistive pathway, the choice of local root water uptake method affects the water potential distribution. The change in water potential in the xylem and at the soil-root interface is significantly affected by considering the local hydraulic conductivity drop compared to neglecting the local conductivity drop. The time occurrence of plant stress, which is a measure for the integrated local soil-root interactions, occurs earlier if the local conductivity drop is incorporated. It is, however, very much dependent on root conductivities

and root collar boundary conditions. To investigate this more thoroughly non-uniform and non-constant root hydraulic parameterizations should be analyzed. Additionally, the effect of the soil texture may not be disregarded in these simulations as it influences the time span to reach stress conditions. Moreover, it affects the relative differences in water potential distribution (in the soil, at the soil-root interface and in the xylem) between considering and not considering the local conductivity drop. It furthermore seems that sink term patterns, for flux boundary conditions at the root collar, are not largely affected by soil discretization. To understand sink term patterns or locally modelled uptake mechanisms near plant roots in detail, new non-invasive techniques like NMR (Pohlmeier *et al.*, 2008) are needed.

# Chapter 4

# A grid refinement approach for a 3D soil-root water transfer model*

## 4.1 Objectives

In this chapter a grid refinement approach is developed based on *a priori* root information that can be used in either a static or dynamic way. First a regular fine grid (reference grid) is compared with three regular coarser grids and three static refined grids based on *a priori* root information in terms of accuracy and computational time for a given soil-root scenario. Furthermore, an obtained static grid using *a priori* information is compared and validated with grids obtained by an *a posteriori* error estimate, that was deduced for the 3D water flow equation. In order to compare both methods the *a posteriori* refinement method is adapted to generate 'static' grids. Finally, we address the usage of dynamic *a priori* refinement techniques for the presented 3D soil-root water flow model.

## 4.2 Introduction

For a variety of environmental and agricultural purposes, such as irrigation management or yield prediction under water scarcity conditions, the understanding of root water uptake processes is of importance. Model development have lead to 3D soil-root water flow models that describe the relationship between water flow in soil and the uptake of water by plant roots (Javaux *et al.*, 2008). In such models the root structure is independently coupled

*adapted from T. Schröder, L. Tang, M. Javaux, J. Vanderborght, B. Körfgen, and H. Vereecken (2009). A grid refinement approach for a 3D soil-root water transfer model, Water Resources Research, submitted

to the soil grid that is used for the numerical solution of the soil water flow equation, i.e. the Richards equation. Because of more accurate measurement techniques (Pohlmeier *et al.*, 2008) and improved root growth and root architecture models (Pagès *et al.*, 2004) more detailed root architectures can be obtained. Furthermore, to acquire high resolution soil water potentials and velocity profiles (for solute transport) a fine soil discretization is needed (Schröder *et al.*, 2009). As a consequence, computational costs increase largely for estimation of the water potentials in the soil domain enclosing detailed root structures. Grid refinement techniques can be used to reduce computational costs by increasing the spatial resolution at locations where high gradients in soil water potential and pore water velocity exist, and using a coarser discretization at other locations (Mansell *et al.*, 2002). This effectively decreases the number of elements used in the numerical grid but at the same time keeps the high spatial resolution in parts of the domain where gradients are large.

A generally used method for grid refinement is the *a posteriori* error estimate (Babuška and Rheinboldt, 1978). In this method the error between exact and approximated solution for the elements of the soil grid is calculated after the linear system of equations is solved. If the error exceeds a certain threshold value the element is refined. The *a posteriori* error estimate is a dynamic approach where the soil resolution increases (or decreases) over time. Dynamic approaches could e.g. be used for modelling root growth. For 2D soil grids with a 2D root growing system Wilderotter (2003) imposed such a scheme. A second method for grid refinement is the usage of *a priori* information. In root water uptake models, it is expected that, due to transpiration, large soil water potential gradients will occur around active roots. Therefore, a finer soil discretization in the vicinity of roots is required (see e.g. Schröder *et al.*, 2008). An *a priori* grid can be developed based on the root architecture with finer elements near roots and coarser elements further away. *A priori* refinement can either be used in a static or dynamic way. A static grid is defined as a grid that does not change over time and is acquired after considering the total root structure. A dynamic grid is only based on that part of the root structure that is active and takes up water, and is time dependent.

The problems that arise with refinement techniques for coupled 3D soil-root water flow models are related to the size of the soil discretization. First, the Richards equation is only valid for a soil discretization larger than the representative elementary volume of the soil texture (Bear, 1972). Second, if very small soil elements are used the volume of soil around a root is very small, such that the ratio of the uptake rate to the volume of soil (i.e.

the sink term) becomes very large causing the system of equations to diverge. Therefore a theoretical and methodological limit exists in the minimum dimension of a soil element.

## 4.3 Methods

### 4.3.1 3D macroscopic water flow model in soil and roots

The model of Javaux *et al.* (2008) consists of two interacting systems: the soil matrix and the root architecture. The soil system is discretized into cubes that are again divided into six linear tetrahedral elements of equal shape, to be used for numerical interpolation of the Richards equation. The root system is divided into nodes connected by segments. For both systems a set of equations is solved in terms of water potential and both are coupled via the sink term $S$ in the Richards equation, see Javaux *et al.* (2008) for more details. The boundary conditions for the plant root system are a transpiration rate or a water potential at the root collar, and a soil water potential at the soil-root interface enabling calculation of the water potential within the roots. Stress is defined when the water potential at the root collar is lower than a limiting water potential value. From this point on the water potential is kept constant at the root collar so that the simulated actual transpiration rate becomes smaller than the potential transpiration rate.

Radial soil-root water flow $J_r$ [cm$^3$ d$^{-1}$] is given by

$$J_r = L_r^* A_r(\psi_{int} - \psi_{xylem}) \tag{4.1}$$

where $L_r^*$ is the radial root conductivity [d$^{-1}$], $A_r$ [cm$^2$] the root outer surface and $\psi$ [cm] represents the water potential expressed as hydraulic head at the soil-root interface ($\psi_{int}$) and in the xylem ($\psi_{xylem}$) respectively. The outer root surface is defined by $A_r = 2\pi r_{int} l_r$, with $r_{int}$ [cm] the root radius and $l_r$ [cm] the length of the root segment. The water potential at the soil-root interface is estimated by a distance-based weighting function of the water potential in the surrounding soil nodes. The sink term [d$^{-1}$] of a soil cube $j$ is calculated by

$$S_j = \frac{\sum_{k=1}^{n_j} J_{r,k}}{V_j} \tag{4.2}$$

where the nominator represents the sum of all the radial soil-root fluxes of the $n_j$ root nodes located inside a soil cube $j$ and $V_j$ [cm$^3$] is the volume of the $j^{th}$ soil cube. A root

node is defined as the center of a root segment at which water exchange is allowed. The sink term is then distributed upon the soil nodes $i$ representing the bulk soil

$$S_i = S_j \frac{\frac{(\psi_i - \psi_{int})}{dist_i}}{\sum_{k=1}^{8} \frac{(\psi_k - \psi_{int})}{dist_k}}, \qquad \text{for } i = 1, \ldots, 8 \tag{4.3}$$

where *dist* is the distance from the soil node $i$ to the soil-root interface.

For each timestep of the simulation first the root system is solved, after that the soil system and again the root system in an iterative way. If the changes in both systems are lower than imposed tolerance criteria, for water content and water potential regarding the soil system and for xylem water potential regarding the root system, the final solution for this timestep is found and the simulation continues with the next timestep.

### 4.3.2 *A priori* refinement

The initial, regular coarse grid is divided into cubes which are again divided into elements. The *a priori* refinement technique is applied to the soil cubes not the elements. Firstly, to enable the usage of Eq. 4.2. Secondly, because of lower computational costs of routines that are needed for Eq. 4.1 and 4.2 when using cubes instead of elements. As the discretization size of a cube is limited a multi-level refinement technique up to a minimal grid size is employed. This technique is based on bisections of the initial coarse grid, without additional coarsening. A 2-level refinement scheme is demonstrated in Fig. 4.1 using the known root information. Consider a root node positioned randomly in a soil cube as given in Fig. 4.1A. Then we

1. bisect this cube in eight parts (Fig. 4.1B)
2. identify the sub-cube containing the root node
3. bisect the identified cube in additional eight cubes (Fig. 4.1C)

For a static grid this procedure is performed for all root nodes in the given soil domain, for a dynamic grid only a selection of root nodes is considered. After this procedure a first refined grid based on the *a priori* root information is gained.

Due to the multi-level refinement smaller soil cubes were generated with so called slave nodes. Slave nodes are soil nodes that are not connected to another soil node in all available directions of the 3D grid. Master nodes, on the other hand, are connected in all possible

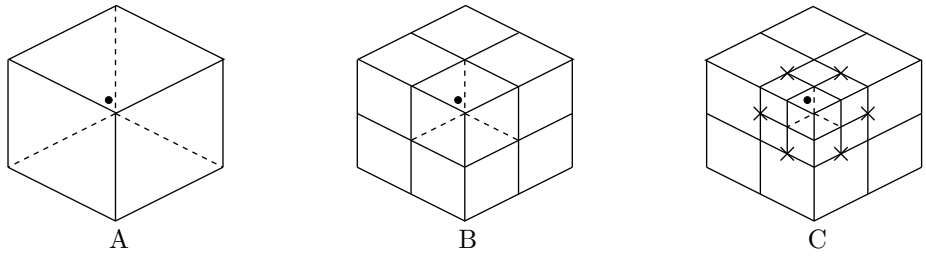


**Fig.** 4.1: Bisection of a soil cube. Graph A shows a coarse cube with a root node (black dot). This cube is splitted in equal parts and the refined cube (B) is obtained. This cube is divided again in the sub-cube containing the root node and leads to the refined grid (C). In (C) slave nodes (crosses) are denoted, but only those at the drawn outer soil surfaces.

directions, i.e. in 6 directions if the soil node is not located at the soil boundary domain. Slave nodes are located on the six faces of a coarser soil cube bounding its sub-cubes (crosses in Fig. 4.1C). Two problems occur when using the multi-level refinement technique. The first problem is related to the allocation of a sink term to a soil node in the 3D model. In the case of regular grids (all master nodes) each soil node has a predefined volume of soil including nodes located at the soil boundary domain. This volume of soil is used in Eq. 4.2 to estimate the sink term obtained from the radial water flow of the root system. Allocation of a soil volume to a slave node is rather complicated, as the volume of soil is not necessarily equal to the volume of the cubes the slave node belongs to. An example is illustrated in Fig. 4.1C. A slave node belongs in this example to two fine soil cubes, however, it has also influence on the larger adjacent cube without being an actual node of this cube. The grid is therefore extended around the initial multi-level refined grid to transform a slave node, that has been allocated a sink term, into a master node. Hereto neighboring cubes, adjacent to the cube with the slave node, with a refinement level larger than the minimal refinement level are refined to this minimal level. The second problem deals with the derivative of the solution variable (water potential) at the interface between coarser and finer cubes. After the initial multi-level refinement only soil cubes with root nodes in it are refined. It may very well occur that an unrefined coarser soil cube is located next to a refined coarser cube (where the difference in level of refinement is two or higher). In this case large jumps in the derivative of the solution variable are expected. To predict a smooth gradient throughout the soil the transition from coarser cubes to finer cubes and vice versa is restricted to a stepsize of one in the level of refinement.

### 4.3.3 Dynamic *a priori* refinement based on active root segments

A static *a priori* grid is gained if all root nodes are considered for refinement of the soil grid. It would be ideal for assuming that all root nodes take up water simultaneously. This is not the case in reality though, only part of the root system is active (Passioura, 1980) as is shown by simulations of Javaux *et al.* (2008) and Schröder *et al.* (2009). Thus, the disadvantage of the static grid is that the number of soil nodes is generally overestimated. Furthermore, the root system may grow and finer soil cubes may be required. Therefore a dynamic approach is introduced. Initially the simulation is started with a coarse grid. After the root system is solved, only those root nodes with a radial soil-root water flow are considered and refinement is performed as in the previous section. Furthermore a criterion is introduced such that refinement is performed again if this criterion is exceeded. For each timestep the difference in radial soil-root water flow between the current timestep and the one on which previous refinement was considered, is calculated. However, only for those root nodes around which the soil is not yet refined. If the sum of the absolute differences is larger than 5% of the total absolute sum of the radial soil-root water fluxes (at the current timestep) then refinement is allowed. Refinement can be performed in addition to the already existing grid. However, root water uptake patterns may shift largely between soil layers (Li *et al.*, 2002a; Schröder *et al.*, 2008) and the refined grid may have soil cubes that equal the minimum discretization size but where no refinement is actually desired, as the roots do not take up water anymore. Therefore the initial coarse grid is taken as point of departure for each refinement and refinement is performed for only those soil cubes that have root nodes with a radial soil-root flow unequal to zero.

### 4.3.4 *A posteriori* refinement

The *a posteriori* error estimate is a widely used dynamic method for grid refinement in soil water flow models (Mansell *et al.*, 2002). Based on the *a posteriori* error estimate a grid that produces the smallest error between the approximated and exact solutions for the current time step can be created. The major disadvantage is that the obtained grid is not fulfilling the criteria that were posed for the 3D soil-root model, namely the slave nodes should not have a denoted sink term and the transitions in grid size between two adjacent soil cubes should not exceed a stepsize of one.

Here the *a posteriori* error estimate is used as a tool to validate the *a priori* refinement method. A derivation of the *a posteriori* error estimate is given in Appendix B and a short

description is given hereafter. After the system of equations is solved with some method the error of an element $T$ can be determined. The error depends on the residual values of the vertices of an element (element residual) and on the residual values of the faces of an element (jump residual). From these residuals the so called local error indicator ($\eta_H$) of an element can be deduced. Another important concept, oscillation ($osc_H$), accounts for information missed by the averaging process associated with the employed finite element method. The local error indicator and the oscillation are important parameters for *a posteriori* refinement. If refinement is required, by evaluation of a threshold value, then elements can be marked based on these two parameters. The first marking strategy selects the minimal subset of elements $\hat{T}_H$ of the mesh $\mathcal{T}_H$ such that

$$\sum_{T \in \hat{\mathcal{T}}_H} \eta_H(T)^2 \geq \theta_E^2 \eta_H(\Omega)^2 \tag{4.4}$$

with $0 < \theta_E < 1$ and $\Omega$ consists of all elements. The second strategy replaces in Eq. (4.4) the error with oscillation

$$\sum_{T \in \hat{\mathcal{T}}_H} osc_H(T)^2 \geq \theta_o^2 osc_H(\Omega)^2 \tag{4.5}$$

with $0 < \theta_o < 1$. Note that, equivalent to the multi-level refinement strategy, the soil cubes with the marked elements are refined.

### 4.3.5 Simulation scenarios

A soil-root scenario is defined to demonstrate the refinement techniques discussed in this paper. The soil-root scenario consists of a soil column with dimensions 10 by 10 by 34 cm. The texture is a loamy soil with parameters $\theta_r = 0.08$ cm$^3$ cm$^{-3}$, $\theta_s = 0.43$ cm$^3$ cm$^{-3}$, $K_s = 50$ cm d$^{-1}$, $\alpha = 0.04$ cm$^{-1}$, $\lambda = 0.5$ and n = 1.6 (Carsel and Parrish, 1988). The Mualem-van Genuchten parametrization (Van Genuchten, 1980) is used to evaluate the soil characteristics $K(\psi)$ and $\theta$ needed by the Richards equation. The soil is considered homogeneous with an initial water potential of -300 cm throughout the soil. The root structure is a 500 h old root generated by the model of Somma *et al.* (1998) and consists of 9488 root segments. Root system hydraulic parameters dependent on root segment age, for radial as well as axial flow within the roots, were taken from Doussan *et al.* (1998b). Only water flow, neither solute transport nor root growth is simulated. Zero fluxes at

the top, bottom and lateral boundaries of the soil domain are imposed. Two type of root collar boundary conditions are used for the simulations. First, a constant water potential at the root collar equal to -15000 cm is imposed. Simulations are performed over 5 days and the amount of water taken up by the roots, expressed in the actual transpiration rate, is evaluated. Second, a constant flux at the root collar equal to 15 $cm^3$ $d^{-1}$ is imposed. The transpiration of water by the plant causes a continuous water uptake by the roots and the simulation is stopped if the xylem water potential reaches a certain water potential threshold value at the root collar (-15000 cm), thereby simulating water stress conditions. This boundary condition allows for investigation of soil-root interactions in locally dry soil regions that will develop around roots (Schröder *et al.*, 2009).

### Comparison of static irregular *a priori* grids with regular grids

Several scenarios were simulated to compare the performances of the model with irregular versus regular soil grids. Table 4.1 summarizes the 7 scenarios. Scenarios 1-4 are the standard non-refined cases (0-level refinement) with different levels of discretization. Cases 5-7 represent scenarios in which static *a priori* refined grids were generated: based on the total root architecture and which do not change over time. These cases differ by their initial soil discretization and their level of refinement. After refinement, grids are generated that end up with fine soil cubes (0.25 by 0.25 by 0.25 cm) around roots, equal to the minimum soil discretization that was set for scenario 1; reference scenario. Both flux and water potential boundary conditions were used to compare scenario 2-7 with the reference grid configuration in terms of accuracy and computational time.

**Table** 4.1: The grid configurations that are evaluated for the soil-root scenario.

| Scenario | Type of refinement | Initial soil discretization [cm] |
|---|---|---|
| 1 | 0-level refinement | 0.25 by 0.25 by 0.25 (reference) |
| 2 | 0-level refinement | 0.5 by 0.5 by 0.5 |
| 3 | 0-level refinement | 1 by 1 by 1 |
| 4 | 0-level refinement | 2 by 2 by 2 |
| 5 | 1-level refinement | 0.5 by 0.5 by 0.5 |
| 6 | 2-level refinement | 1 by 1 by 1 |
| 7 | 3-level refinement | 2 by 2 by 2 |

### *A priori* versus *a posteriori* refinement

The second comparison that is performed is between a static *a priori* grid (scenario 6, Table 4.1) and *a posteriori* grids. The *a posteriori* refinement method is adapted for this purpose. Root water uptake is imposed for all root segments of the root system, with a sink value equal to 1e-3 $d^{-1}$. The objective here is to investigate whether the static grid obtained with the *a priori* refinement method is similar to the one obtained with the well known *a posteriori* error estimate. Generation of the grid by using an *a posteriori* error estimator starts with an initial coarse grid of 1 by 1 by 1 cm soil cubes and refinement is allowed upto a minimum discretization size (0.25 by 0.25 by 0.25 cm). Marking procedures are alternated between local error (Eq. (4.4)) and oscillation (Eq. (4.5)) for 4 cases, see Table 4.2. With these cases the effect of the marking sequences can be evaluated. If

**Table** 4.2: The *a posteriori* scenarios for different marking sequence parameters to be used for a 2-level refinement scheme for the soil-root scenario with a flux type root collar boundary condition.

| Scenario | Type of refinement | $\theta_E$ | $\theta_o$ |
|---|---|---|---|
| post 1 | *a posteriori* | 0.6 | 0.4 |
| post 2 | *a posteriori* | 0.6 | 0.3 |
| post 3 | *a posteriori* | 0.5 | 0.5 |
| post 4 | *a posteriori* | 0.5 | 0.2 |

a new grid is gained after refinement, the same simulation time is rerun until a grid is obtained where all soil cubes with a root segment, that takes up water, equal the minimum discretization size. This methodological criterion is similar as the one for static *a priori* refinement, and is used in order to get a fair comparison between the two refinement methods. However, based on mathematical rules Eq. (B.11) should be evaluated for the *a posteriori* refinement technique. After the final grid is acquired it is expanded to ensure mass conservation (slave nodes with a denoted sink are extended to master nodes). From this moment on we let the model run similarly to the static *a priori* grid using the flux root collar boundary condition. It may seem trivial to compare these cases but these comparisons are performed mainly for validation purposes of the *a priori* grid. Secondly, information is gained on the accuracy of simulations with *a posteriori* grids, on the effect of the marking sequences and on the computational time to create *a priori* versus *a posteriori* grids.

Dynamic *a priori* refinement based on active root segments

A third comparison evaluates dynamic *a priori* refinement based on active root segments. We consider a 2-level refinement scheme (equivalent to scenario 6 of Table 4.1) and again we impose the flux boundary condition of 15 $cm^3$ $d^{-1}$ at the root collar. The results are compared in terms of accuracy and computational time with the reference case (scenario 1 of Table 4.1). Furthermore they are compared with the results obtained using static *a priori* grids.

## 4.4 Results and discussion

### 4.4.1 Comparison of static irregular *a priori* grids with regular grids

First the scenario with the water potential boundary condition at the root collar is compared for the seven grid configurations of Table 4.1. Such root collar boundary condition generates a decrease of the root collar flux over time since the water potential gradient between the root xylem tissue and the soil diminishes with soil water depletion. This is observed in Fig. 4.2. The area under the curves equals the total amount of water that is taken up from the soil. Evaluating the coarse grid configurations (scenarios 2 (magenta), 3 (yellow) and 4 (cyan)) a less sharp decrease in actual transpiration rate is noticed compared to the reference scenario (black line), meaning that more water is extracted from the soil. Thus, following Eq. (4.1), the water potential estimate at the soil-root interface has a higher value than the reference scenario. This was expected from results shown by Schröder *et al.* (2008). The *a priori* refined grids (scenarios 5 (green), 6 (red) and 7 (blue)) on the other hand are hardly distinctive with the reference case, indicating that the plant architecture indeed provides a very good estimate for the locations where high soil water potential gradients will occur.

The accuracy of the solutions obtained with the different grid configurations can be tested over the whole water potential range using a flux boundary condition at the root collar. We are especially interested in dry soil regions that develop around roots over time. Soil water potential and xylem water potential distributions were compared at three simulation times (0.5, 4 and 5.4 d). The first simulation time (0.5 d) depicts wet soil conditions. At the second simulation time (4 d) the soil around the roots is much dryer and at the third simulation time (5.4 d) the limiting threshold value at the root collar is almost reached for the *a priori* refined scenarios and the reference case. From a soil

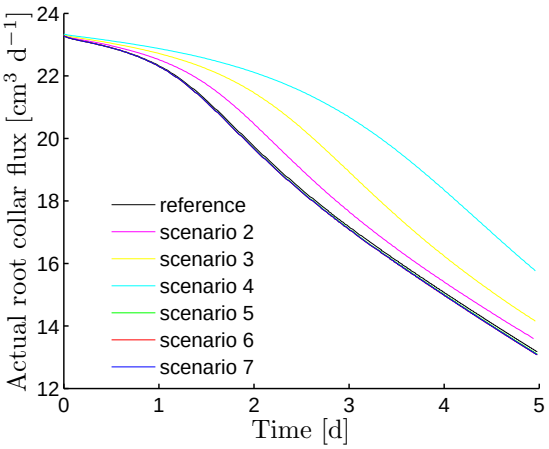


**Fig.** 4.2: Actual root collar fluxes for the simulated scenarios 1–7 of Table 4.1 with a water potential root collar boundary condition.

point of view we compare the root mean square error (RMSE) of the soil water potentials of scenario 2-7 with the reference scenario at an arbitrary x-y cross-section (z = -2 cm) in the soil column. Note that the root length density is high in this cross-sectional plane (not shown). The RMSE values are denoted in Table 4.3. At day 0.5 the soil is still very wet and low RMSE values are observed. Larger differences in RMSE values between the coarse discretization and the *a priori* refined grids are already observed. In dryer soil regions the RMSE of scenario 2 (0.5 by 05 by 0.5 cm) is about a factor of 6 higher than the corresponding *a priori* refined grid (scenario 5). Scenario 3 (1 by 1 by 1 cm) and scenario 4 (2 by 2 by 2 cm) differ with a factor larger than 10 and 20, respectively, compared to their *a priori* refined grids. The coarse discretizations are not predicting the soil water potential distributions accurately. Maximum and mean errors in xylem water potential for

**Table** 4.3: Root mean square errors [cm$^2$] of the soil water potentials in a x-y cross-section at z = -2 cm at simulation day 0.5, 4 and 5.4 d. The errors are obtained by comparing the simulated scenarios of Table 4.1 with the reference scenario.

| | Scenario | | | | | | |
|---|---|---|---|---|---|---|---|
| | reference | 2 | 3 | 4 | 5 | 6 | 7 |
| RMSE at t = 0.5 d | - | 2.5 | 7.7 | 15.7 | 0.9 | 1.0 | 1.0 |
| RMSE at t = 4 d | - | 133.6 | 307.6 | 469.9 | 22.2 | 29.8 | 28.7 |
| RMSE at t = 5.4 d | - | 216.0 | 472.4 | 880.8 | 33.5 | 45.2 | 43.6 |

the whole root structure are given in Table 4.4 for the three different simulation times. At day 0.5 (wet soil conditions) the coarse grid configurations have very large maximal errors (>35%). The mean error though is still low (below 5%), except for scenario 4. At

day 4 and 5.4 (dryer soil conditions) the mean errors of the coarse discretizations become larger than 5%. The *a priori* refined grids, conversely, show maximum errors at simulation time 5.4 of below 5.5% and mean errors near and below 2.5%. The errors observed for the *a priori* refined grids (scenario 5-7), even in local dry soil conditions, can be considered marginal.

Table 4.4 shows furthermore the total computational time ($T_c$) and number of soil nodes used for each simulation. Regular coarse grids are fast, even scenario 2 (0.5 by 0.5 by 0.5 cm) needs only 14% of the time needed for the reference scenario. However, they give poor accuracy as observed before. On the other hand, *a priori* refined grids take approximately half the computational time of the reference grid (for this example), while keeping a very good accuracy for the water potential prediction as compared to the fine regular grid (reference). The lowest errors, from a soil and root point of view, are obtained with scenario 5 (1-level refinement scheme). Note that the number of soil nodes that were generated by the refinement approaches 5-7 differ, dependent on the initial soil spatial discretization and the level of refinement. No linear relation between the number of soil nodes and the soil spatial resolution, as was the case for regular grid configurations, can be found anymore. For this root structure scenario 6 (2-level refinement) generates the fewest soil nodes. Moreover, the total computational time is the lowest.

**Table** 4.4: Xylem water potential ($WP_x$) errors for the total root structure at simulation day 0.5, 4 and 5.4 and computational time $T_c$ for the simulated scenarios of Table 4.1 compared to the reference scenario. Furthermore the number of soil nodes for each grid configuration is given.

| | Scenario | | | | | | |
|---|---|---|---|---|---|---|---|
| | reference | 2 | 3 | 4 | 5 | 6 | 7 |
| max error in $WP_x$ [%] at t = 0.5 d | - | 35.1 | 41.0 | 46.0 | 0.7 | 0.8 | 0.8 |
| mean error in $WP_x$ [%] | - | 1.1 | 3.3 | 6.5 | 0.3 | 0.3 | 0.3 |
| max error in $WP_x$ [%] at t = 4 d | - | 40.8 | 68.2 | 78.3 | 3.4 | 4.6 | 4.5 |
| mean error in $WP_x$ [%] | - | 5.2 | 12.4 | 22.2 | 1.4 | 1.9 | 1.8 |
| max error in $WP_x$ [%] at t = 5.4 d | - | 39.2 | 64.9 | 81.3 | 3.9 | 5.5 | 5.2 |
| mean error in $WP_x$ [%] | - | 6.8 | 16.5 | 27.9 | 1.7 | 2.4 | 2.3 |
| $T_c$ compared to reference [%] | 100 | 14 | 6 | 4 | 47 | 46 | 49 |
| Number of soil nodes | 230297 | 30429 | 4235 | 648 | 78312 | 69760 | 72113 |

### 4.4.2 *A priori* versus *a posteriori* refinement

The static *a priori* grid from scenario 6 (2-level refinement, Table 4.1) is visually compared to two obtained grids using the adapted *a posteriori* error estimate in Fig. 4.3. The adapted *a posteriori* error estimate creates a grid based on the uptake of water by all root

segments. The left graph shows a transparent XZ view for the *a priori* grid, the middle graph of the *a posteriori* grid (post 1) with a $\theta_E$ of 0.6 and $\theta_o$ of 0.4 and the right graph of the *a posteriori* grid (post 4) with a $\theta_E$ and $\theta_o$ of respectively 0.5 and 0.2. The *a posteriori* grids show that indeed soil voxels have a finer discretization near roots where larger water potential gradients are observed. In total 99% of both *a posteriori* refined grids corroborate with the *a priori* refined grid. On the other hand we notice for both scenarios differences in transition from coarser to finer soil cubes, other than a stepsize of one. Furthermore, the first depicted *a posteriori* grid (post 1, $\theta_E = 0.6$ and $\theta_o = 0.4$) has more refined soil cubes in the lower soil regions compared to the second depicted *a posteriori* acquired grid. Note that there were no flux boundary conditions at the soil boundaries. The major cause of these differences is the sensitivity of the marking sequences. The higher the instituted value for $\theta_E$ or $\theta_o$ the more soil elements are selected for refinement. The results of scenario post 1 point out that after selection of those elements with a high error, other elements with lower errors were selected as well. These elements were located further away from the root structure, where no high water potential gradients and errors reside. For the 3D soil-root water transfer model the choice of the marking sequence parameters is not straightforward. This can furthermore be observed from the number of soil nodes of the other acquired *a posteriori* grids in Table 4.5. Both the error and oscillation marking sequence parameters affect the number of refined cubes largely. The first *a posteriori* grid (post 1) creates a mesh with over 100.000 nodes, whereas the grid with a $\theta_E$ of 0.5 and $\theta_o$ of 0.2 (post 4) is much closer to the number of soil nodes of the *a priori* obtained grid. From all grids the *a priori* grid is with respect to the spatial distribution more optimal than the *a posteriori* grids. Not only because a minimum number of soil nodes is generated, but also because transitions in soil cubes from coarse to fine and vice versa differ only a stepsize of one.

One of the adaptations for the usage of the *a posteriori* error estimate was that refinement was stopped after all soil cubes with a root segment, that takes up water, equal the minimum discretization size. This adaptation can be tested by analyzing the local error indicator in Eq. (B.11). It was observed that the difference in local error indicator between the previous refined grid and the current refined grid started to converge to a small value. Furthermore, the maximum error was initially very large for the coarse soil discretization and was reduced for each time the grid was refined. When finally all soil cubes with root nodes in it equalled the minimum discretization size an acceptable maximum error, in comparison to the estimated soil water potential, was calculated. Moreover, there was no indication to interrupt the *a posteriori* refinement procedure earlier than the methodological imposed criterion that was implemented. This indicates that the criterion we imposed is not a bad assumption. Furthermore, the local error indicator was derived separately for the *a priori* obtained grid and showed that the maximum error was acceptable as well,

in comparison to the estimated soil water potential. This indicates furthermore that *a priori* grids lead to a reduction in the error between exact and approximated solutions, compared to a coarse grid configuration, and that refinement was performed at correct locations where soil water potential gradients were expected to be larger, i.e. near roots.

After the 'static' grid is obtained with the adapted *a posteriori* error estimate we let the simulation run for a flux root collar boundary condition until stress is reached. A comparison of the xylem water potential error in Table 4.5 at the three simulation times (0.5, 4 and 5.4 d) shows that the errors obtained with the *a posteriori* refinement approach (compared to the reference scenario) are within range of the errors acquired with the *a priori* grid. Mostly they are slightly higher, however, for the post 3 case ($\theta_E, \theta_o = 0.5$) the xylem water potential errors are slightly lower. This is mainly caused by the large difference in number of soil nodes between those scenarios, secondly by the location where soil nodes are refined. The latter is dependent on $\theta_E$ and $\theta_o$ parameters. If in a soil layer (perpendicular to the axial direction) more fine soil cubes are generated the water potential gradient will be predicted steeper compared to the case where more coarse soil cubes are present, caused by the linear interpolation in elements (Schröder *et al.*, 2008). More important is the comparison of the computational time in Table 4.5. The computational time is significantly affected, it is even larger than the reference scenario for all *a posteriori* scenarios. This is mainly caused by the computational routines to estimate the local error for each element, furthermore because of additional routines to obtain a grid that ensures conservation requirements. For the *a posteriori* scenario 4 ($\theta_E = 0.5$, $\theta_o = 0.2$) the time to generate the static grid with the adapted *a posteriori* error estimate is about 10 times longer than the time needed using the *a priori* approach.

**Table** 4.5: Xylem water potential ($WP_x$) errors for the total root structure at simulation day 0.5, 4 and 5.4 d and computational time $T_c$ for the simulated *a posteriori* refinement scenarios (Table 4.2) and scenario 6 of Table 4.1 (*a priori* grid) compared to the reference scenario. Furthermore the number of soil nodes for each grid configuration is given.

| | Scenario | | | | | |
|---|---|---|---|---|---|---|
| | reference | pre 6 | post 1 | post 2 | post 3 | post 4 |
| max error in $WP_x$ [%] at t = 0.5 d | - | 0.8 | 0.6 | 0.6 | 0.5 | 0.7 |
| mean error in $WP_x$ [%] | - | 0.3 | 0.3 | 0.3 | 0.3 | 0.3 |
| max error in $WP_x$ [%] at t = 4 d | - | 4.6 | 5.6 | 5.7 | 3.8 | 5.0 |
| mean error in $WP_x$ [%] | - | 1.9 | 2.3 | 2.3 | 2.0 | 2.0 |
| max error in $WP_x$ [%] at t = 5.4 d | - | 5.5 | 7.0 | 6.9 | 5.6 | 5.8 |
| mean error in $WP_x$ [%] | - | 2.4 | 2.8 | 2.9 | 2.3 | 2.5 |
| $T_c$ compared to reference [%] | 100 | 46 | 260 | 210 | 280 | 170 |
| Number of soil nodes | 230297 | 69760 | 106831 | 93220 | 100371 | 75151 |

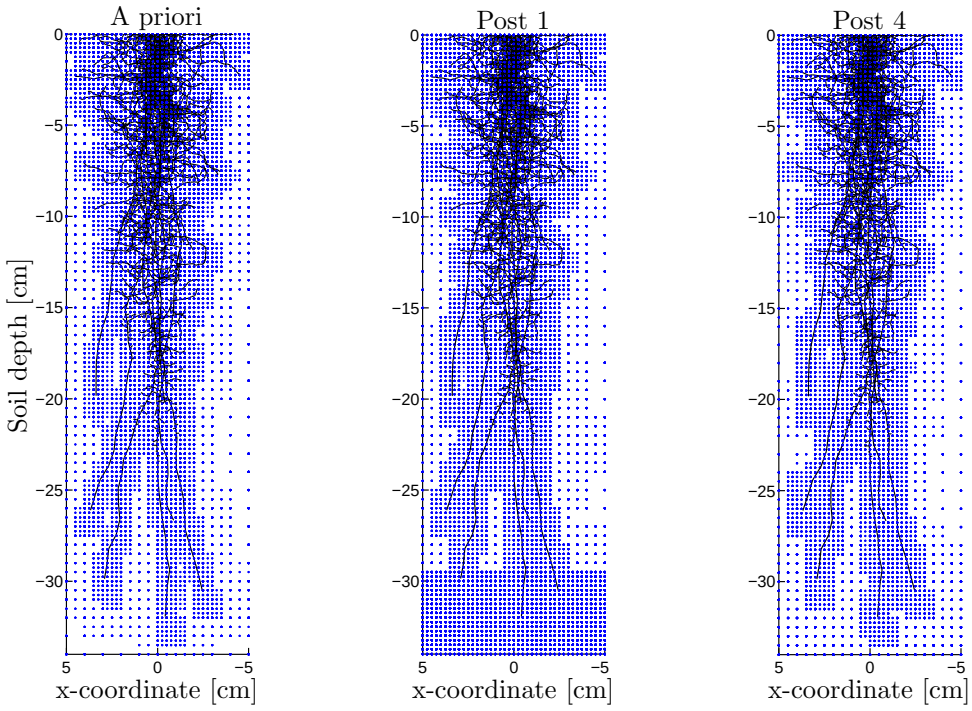


**Fig.** 4.3: Left: XZ aspect of the *a priori* grid (2-level refinement; scenario 6). Middle: XZ aspect of the *a posteriori* grid with $\theta_E = 0.6$, $\theta_o = 0.4$ (scenario post 1 of Table 4.2). Right: XZ aspect of the *a posteriori* grid with $\theta_E = 0.5$ and $\theta_o = 0.2$ (scenario post 4 of Table 4.2). The solid lines denote root branches, whereas the dots represent soil nodes.

### 4.4.3 Dynamic *a priori* refinement based on active root segments

Simulations were performed for flux root collar boundary conditions. The errors in xylem water potential and the computational time of the dynamic *a priori* grid scenario, where refinement is based on the distribution of the active roots, are compared to the reference scenario in Table 4.6. Furthermore, the static *a priori* grid (scenario 6, Table 4.1) is given to facilitate evaluation. Striking is the difference in maximum water potential error. Despite the fact that only those soil cubes are refined with a root segment that takes up water, the water potential gradient estimation from the outer soil column towards the roots is affected. It is the same principle as was mentioned in the previous section. In the dynamic approach more coarse cubes are available in a horizontal soil layer and the predicted water potential gradient from the soil outer boundary towards the root segments is calculated less steep, compared to the reference scenario. Although the maximum xylem water potential errors are rather large in the dynamic approach the mean errors are still below 5% and acceptable. Furthermore, the errors are lower than the errors observed for the coarse grid configurations (Table 4.4). The dynamic approach based on *a priori*

root information seems to be a suitable approach for simulating quickly and with high enough accuracy. The computational time is reduced by 20% compared to the static *a priori* grid. This is mainly caused by the reduction in number of soil nodes. Approximately 50% less soil nodes were initially generated with the dynamic approach. Note that the grid was furthermore constant over time, as the observed differences in radial soil-root water flow (for the dynamic criterion) were less than 0.001%, so that the criterion that was used to decide on grid refinement did not indicate a need to refine additionally. The dynamic approach can be applied on large soil and root structures that can be run on a single processor for a coarse soil discretization, but not for a regular fine soil discretization, or with the static approach. This is however dependent on the type of scenario and the available computer resources. Furthermore, root growth can easily be modelled with the dynamic refinement scheme.

**Table** 4.6: Xylem water potential ($WP_x$) errors for the total root structure at simulation day 0.5, 4 and 5.4 d and computational time $T_c$ for the simulated dynamic *a priori* refinement scenario compared to the reference scenario. Furthermore, the static *a priori* scenario 6 (Table 4.1) is denoted for comparison purposes.

| | Scenario | | |
|---|---|---|---|
| | reference | static *a priori* | dynamic *a priori* |
| max error in $WP_x$ [%] at t = 0.5 d | - | 0.8 | 4.3 |
| mean error in $WP_x$ [%] | - | 0.3 | 0.7 |
| max error in $WP_x$ [%] at t = 4 d | - | 4.6 | 10.3 |
| mean error in $WP_x$ [%] | - | 1.9 | 2.8 |
| max error in $WP_x$ [%] at t = 5.4 d | - | 5.5 | 13.9 |
| mean error in $WP_x$ [%] | - | 2.4 | 3.8 |
| $T_c$ compared to reference [%] | 100 | 46 | 37 |

## 4.5 Conclusions

Because 3D soil-root water transfer models cost lots of computational time for accurate prediction of water potential gradients in the soil and root system, different grid refinement techniques were evaluated. Because roots take up water and create large soil water potential gradients around them an *a priori* grid refinement technique was introduced based on the root architecture. It can either be used in a static or dynamic approach.

Results from a soil-root scenario for two different root collar boundary conditions show that the accuracy of static *a priori* refined grids is maintained in comparison to a regular fine grid that serves as a reference. In contrast, regular coarse grids do not predict accurate solutions. Furthermore, due to the reduction of the grid complexity the computational time is reduced largely.

The static grid that was obtained by *a priori* refinement can be obtained using a well recognized *a posteriori* refinement technique (adapted to obtain this static grid), indicating once more

that the *a priori* obtained grid is well predicted at locations were roots reside. The disadvantages of the adapted *a posteriori* refinement technique, though, were firstly that the grids were spatially not as optimal as the *a priori* acquired grids; not a minimum number of soil nodes were generated, and not always a transition in soil cubes from coarse to fine and vice versa differed a stepsize of one. Secondly, no significant gain in accuracy, compared to the results using *a priori* grids, was obtained and thirdly the computational time to gain the static *a priori* grid was much larger than the *a priori* approach. As a consequence the total computational time for performed simulations exceeded the time of the reference scenario, which makes the usage of the adapted *a posteriori* refinement approach in these type of soil-root models questionable. On the other hand, if the point of departure is an *a priori* grid then the *a posteriori* refinement technique could be used whenever soil gradients, further away from the roots, get too large after time, e.g. in soil layers were the average water content is very low or due to rapidly changing soil boundary conditions (Mansell *et al.*, 2002). The latter, however, is implicitly considered in the *a priori* refinement technique. Using the *a posteriori* error estimator the grid could be extended such that a better accuracy could be acquired. Note that the trade off between computational costs of the *a posteriori* error estimator and the gain in accuracy/overall computational time should be minimized.

Because only part of the root system is active a static *a priori* grid overestimates the required number of refined soil cubes. Therefore dynamic refinement is incorporated using the *a priori* refinement technique and shows that with an acceptable accuracy, compared to the reference case, the computational time can be reduced even more. The usage of dynamic refinement can be an advantage for modelling large soil and root structures with high accuracy for which, on single processors, only coarse soil and root discretizations with low accuracy can be run. Furthermore, dynamic methods can easily be used to model root growth, opposed to static refinement methods. In latter case it may occur that new grown roots are located in coarse soil cubes which may be undesirable if they start to take up water.

# Chapter 5

# Synthesis

The uptake of water by roots is still a topic of large debate. Many models have been developed over the years to quantify root water uptake at the microscopic and at the macroscopic scale. Nowadays experimental and model developments allow for the characterization of root water uptake in much higher detail. These advancements have lead to 3D soil-root water transfer models that simulate water flow along water potential gradients in the soil-root continuum. However, the coupling of the soil and root system is not investigated thoroughly. In the available models the soil water potential gradient below the resolution scale of the soil system is neglected. This means that the local water flow from the bulk soil to the soil-root interface is not explicitly considered. This thesis addresses the impact of considering the local hydraulic conductivity drop around roots.

## 5.1 Conclusions

In chapter 2 a microscopic analytical approach was developed to consider the local hydraulic conductivity drop below the soil discretization from the bulk soil to the soil-root interface. Validation with a 2D numerical model showed that the analytical approach matches the numerical model with high accuracy.

The analytical approach was incorporated in the 3D soil-root water transfer model of Javaux *et al.* (2008) for single roots. Simulations were performed for water potential boundary conditions at the root collar and showed that neglecting the local hydraulic conductivity drop below the soil discretization scale has a large effect on the prediction of root water uptake. Especially in the case if the radial root hydraulic conductivity is larger than the local soil hydraulic conductivity. These findings were reinforced by numerical validation using mesh refinement.

In chapter 3 three approaches were introduced to take the analytical approach into account

for multiple roots within a soil voxel. Simulations were performed for flux boundary conditions at the root collar. Compared were five scenarios from which one was a reference scenario (very fine soil discretization), the other four had a coarse soil discretization and incorporated either one of the three local uptake methods or the average approach where the local hydraulic conductivity drop was neglected. The water uptake profiles were hardly distinctive among the simulated scenarios. Estimation of the soil-root interface water potential on the other hand showed significant differences. Especially for regions where the radial root conductivity was larger than the local soil hydraulic conductivity. This corresponds to the observations for single roots in Chapter 2. For the coarse soil discretizations that consider the local conductivity drop lower soil-root interface water potentials, and consequently lower xylem water potentials were estimated, as compared to neglecting the local hydraulic conductivity drop. Finally, a minimum xylem water potential (plant stress) was reached earlier. The simulations with a coarse soil discretization that consider the local conductivity drop do not obtain the same results as the reference scenario. For flux root collar boundary conditions a fine soil discretization is needed as interpolation in and between the soil elements has a much larger effect on the estimation of the soil water potential gradient than incorporation of microscopic effects below the soil spatial discretization.

Accurate prediction of water potential gradients using a fine soil and root discretization for large soil and root systems cost lots of computational time. In chapter 4 a grid refinement approach based on the *a priori* known root structure was developed, either in a static or dynamic way. A comparison was performed between regular coarse grids, static *a priori* refined grids and a reference grid (very fine regular soil grid) for different soil-root scenarios. The accuracy of static *a priori* refined grids was maintained compared to the reference scenario, whereas the accuracy of the coarse grids was not. Moreover, the computational time of the soil-root scenario using static *a priori* grids was largely reduced.

The static grid that was obtained by *a priori* refinement can be obtained using a well recognized *a posteriori* refinement technique (adapted to obtain this static grid), indicating once more that the *a priori* obtained grid is well predicted at locations were roots reside.

Because only part of the root system is active a static *a priori* grid overestimates the required number of refined soil cubes. Therefore dynamic refinement was incorporated using the *a priori* refinement technique and showed that with an acceptable accuracy, compared to the reference case, the computational time can be reduced even more.

## 5.2 Perspectives

In this thesis investigation of root water uptake is based on modelling approaches only. Experiments are performed with methods like NMR (Pohlmeier *et al.*, 2008) or Neutron radiography

(Oswald *et al.*, 2008) to visualize the root structure and to quantify the water content. Extraction of the root skeleton is of importance to use experimental data to test the modelling approaches on the microscopic as well as on the macroscopic scale. Therefore visualization techniques are required that render a 3D connected root structure from a 3D matrix of grey values. Validation of the model requires furthermore inverse modelling techniques. With such techniques the root system can be parameterized to predict highly variable root hydraulic properties.

For optimal usage of inverse modelling techniques the computational time of a forward simulation should be minimized. This can either be done by grid refinement or by parallelization techniques. Chapter 4 dealt with refinement techniques. *A priori* refinement techniques are shown to be adequate for these type of models. Though, simulations may be performed over several days with realistic soil and root boundary conditions that may change rapidly. The *a priori* refinement technique refines the grid near the root structure and at soil boundaries, however, it may be that further away from these locations the soil becomes very dry such that large soil water potential gradients are created. *A priori* refined grids then need further refinement to accurately predict soil water potential gradients. *A posteriori* refinement could be used in combination with *a priori* refinement, though the trade off between computational costs of the *a posteriori* error estimator and the gain in accuracy/overall computational time should be minimized.

Dynamic *a priori* refinement was shown to effectively reduce the computational costs considering only those root segments that are active and take up water. This allows for simulation of large soil and root structures with a good estimation of the soil water potential gradients throughout the soil column. However, memory resources on a single processor are limited. Therefore, parallelization of the coupled soil (Hardelauf *et al.*, 2007) and root system is required. With this technique many calculations are performed simultaneously, operating on the principle that large problems can often be divided into smaller problems, which are then solved concurrently. Due to the usage of multiple processors the computational costs of the total simulation will be largely reduced. An additional challenge is then the incorporation of the static/dynamic refinement scheme in parallel.

One of the main objectives in this research community is the assessment of water flow (and solute transport) on a large scale. To find upscale mechanisms, i.e. effective modelling of detailed processes to be used on a larger scale, more detailed information is needed on local root water uptake mechanisms. In chapter 2 and 3 it was shown that root water uptake was affected largely from the moment that locally the soil hydraulic conductivity was lower than the radial root hydraulic conductivity. In these simulations constant root hydraulic properties were investigated for different root collar boundary conditions. Investigation of non-uniform, non-constant root hydraulic properties for different root branches and plant species should be evaluated.

From the results in chapter 3 it can furthermore be noticed that for flux root collar boundary conditions sink term profiles are hardly affected by different local root water uptake methods. This effect may contribute to a more generalized method for upscaling, independent of soil discretization. However, more investigations should be performed to investigate root water uptake patterns with even denser root structures - using non-uniform and non-constant root hydraulic properties - and for various soil textures. Currently, homogeneous soil textures that assume isotropic soil properties were investigated only. Because the soil is very heterogeneous and may possess anisotropic properties as well, these effects should be investigated in addition.

Another important step in the upscaling approach is the incorporation of multiple plants within the 3D model, to investigate plant competition and the effect on root water uptake.

# Appendix A

# Analytical solutions for water flow from bulk soil to soil-root interface

The radial Richards equation (Eq. (2.1)) combined with the matric flux potential (Eq. (2.2)) $\Phi = \int_{h_{-\infty}}^{h_c} K(h)dh$ is expressed in matric flux potential form as given in Eq. (2.3)

$$\frac{\partial \theta}{\partial t} = \frac{1}{r}\frac{\partial \Phi}{\partial r} + \frac{\partial^2 \Phi}{\partial r^2}$$

No prior information is known about the time dependent volumetric water content. We used the assumption of steady-rate behavior, which means the time derivative term is assumed constant, as proposed by e.g. Feddes and Raats (2004) and De Jong van Lier *et al.* (2006). The common solution is then given by

$$\Phi = \frac{c}{4}r^2 + A\ln r + B \quad \text{and} \quad q = -\frac{\partial \Phi}{\partial r} = -\frac{c}{2}r - \frac{A}{r} \tag{A.1}$$

The parameters c, A and B are obtained via the boundary conditions

$$\text{Inner edge:} \quad q = -\frac{\partial \Phi}{\partial r} = -q_{root}, \qquad r = r_{root} \tag{A.2}$$

$$\text{Outer edge:} \quad q = -\frac{\partial \Phi}{\partial r} = -q_{out}, \qquad r = r_{out} \tag{A.3}$$

$$\text{Outer edge:} \quad h_{out} = h(r_{out}) \qquad : \quad \Phi_{r_{out}} = \int_{h_{-\infty}}^{h_{out}} K(h)dh \tag{A.4}$$

which leads to Eq. (2.4). Note that the vector direction of the flux density is opposite and negative to the radial direction from soil-root interface to bulk soil.

Under plant stress conditions a water potential boundary condition is imposed at the soil-root

interface. The boundary conditions are then written as

$$\text{Inner edge:} \quad h_{root} = h(r_{root}) = h_{lim} \quad : \quad \Phi_{r_{root}} = \int_{h_{-\infty}}^{h_{lim}} K(h)dh \to 0 \tag{A.5}$$

$$\text{Outer edge:} \quad h_{out} = h(r_{out}) \quad : \quad \Phi_{r_{out}} = \int_{h_{-\infty}}^{h_{out}} K(h)dh \tag{A.6}$$

$$\text{Outer edge:} \quad q = -\frac{\partial \Phi}{\partial r} = -q_{out}, \qquad r = r_{out} \tag{A.7}$$

which leads to the solution given in Eq. (2.7).

# Appendix B

# *A posteriori* error estimate for the 3D soil water flow equation

The *a posteriori* error estimate is deduced for the Richards equation

$$\frac{\partial \theta}{\partial t} = \nabla \cdot (K(\nabla \psi + \boldsymbol{e_z})) - S_t \tag{B.1}$$

where $\theta$ is the volumetric soil water content [cm$^3$ cm$^{-3}$], $K(\psi)$ [cm d$^{-1}$] the soil hydraulic conductivity, $S_t$ [d$^{-1}$] the sink term regulating root water uptake, $t$ [d] the time and $\boldsymbol{e_z} = \nabla z$ the unit vector field in the vertical direction. The time derivative of the water content is related to the water potential by $\frac{\partial \theta}{\partial t} = C(\psi)\frac{\partial \psi}{\partial t}$, where $C(\psi)$ [cm$^{-1}$] is the soil capacity. We use an implicit backward Euler scheme that transforms Eq. (B.1) in

$$\frac{\theta_{n+1} - \theta_n}{\triangle t} = \nabla \cdot (K(\nabla \psi_{n+1} + \boldsymbol{e_z})) - S_t \tag{B.2}$$

where the subscript $_n$ denotes the previous time step, the subscript $_{n+1}$ the current time step and $\triangle t$ the time stepsize. Eq. (B.2) can be rewritten as

$$-\nabla \cdot (K \nabla \psi_{n+1}) + \frac{\theta_{n+1}}{\triangle t} = f_n \tag{B.3}$$

where $f_n = \nabla \cdot (K\boldsymbol{e_z}) + {}^{\theta_n}/_{\triangle t} - S_t$.
To find the solution $\psi \in \mathbb{V}$ for each time step we need the weak form of Eq. (B.3) over the domain $\Omega$ such that

$$\mathcal{B}[\psi, v] = \int_\Omega \left( K \nabla \psi \cdot \nabla v + \frac{\theta}{\triangle t} v \right) d\Omega + \int_\Gamma (K \nabla \psi v) \cdot \boldsymbol{n} d\Gamma = \int_\Omega f v d\Omega = \mathcal{F}(v) \qquad \forall v \in \mathbb{V} \tag{B.4}$$

where $v$ is a weight function and $\boldsymbol{n}$ the outward unit vector normal to boundary $\Gamma$. Note that we dropped the time index. The discrete weak form is then given by

$$\mathcal{B}[\psi_H, v] = \mathcal{F}(v) \qquad \forall v \in \mathbb{V}_H \tag{B.5}$$

where $\psi_H \in \mathbb{V}_H$ is the approximated solution.

The weight functions are derived for linear tetrahedral elements (Cheng and Zhang, 2007). Assembling of the system of equations is performed as was done by Šimůnek *et al.* (1995). After the linear system of equations is solved with some method we can evaluate the error that emerges when approximating the solution. Substitution of the error $e_H := \psi - \psi_H$ (difference between exact and approximated solution) into the bilinear form $\mathcal{B}[e_H, v]$ (Eq. (B.5)) and integrate by parts elementwise the so called error representation formula is obtained (Nochetto, 2006)

$$\mathcal{B}[e_H, v] = \sum_{T \in \mathcal{T}_H} \int_T R_T(\psi_H) v + \sum_{S \in \mathcal{S}_H} \int_S J_S(\psi_H) v \qquad \forall v \in \mathbb{V} \tag{B.6}$$

The left part $R_T(\psi_H)$ is associated with the element residual, the right part $J_S(\psi_H)$ with the jump residual; similarly to the left handside of Eq. (B.4).

For a tetrahedral element T of the mesh $\mathcal{T}_H$ the element residual is defined as

$$R_T(\psi_H) = f + \nabla \cdot (K \nabla \psi_H) - \frac{\theta_H}{\triangle t} \tag{B.7}$$

where $\theta_H$ is the water content that belongs to the approximated solution variable $\psi_H$. For the set of interior faces $\mathcal{S}_H$ of the mesh $\mathcal{T}_H$ the jump residual is defined as

$$J_S(\psi_H) = -K \nabla \psi_H^+ \cdot \nu^+ - K \nabla \psi_H^- \cdot \nu^- \tag{B.8}$$

where $S$ is the common side of elements $T^+$ and $T^-$ with unit outward normals $\nu^+$ and $\nu^-$, respectively. From this we can deduce the local error indicator $\eta_H(T)$ by

$$\eta_H(T)^2 := H_T^3 \parallel R_T(\psi_H) \parallel^2_{L^2(T)} + \sum_{S \subset \partial T} H_S^2 \parallel J_S(\psi_H) \parallel^2_{L^2(S)} \tag{B.9}$$

where $H$ stands for the mesh size and $L^2$ is the vector space. The element residual is analog to the residual in linear algebra and describes the relation between the error $e_H$ and residual for the vertices of an element. The jump residual evaluates the boundaries of the elements.

Another important concept, oscillation, accounts for information missed by the averaging process associated with the finite element method. The oscillation on the elements $T \in \mathcal{T}_H$ is

defined by

$$osc_H(T)^2 := H_T^3 \parallel R_T - \overline{R_T} \parallel^2_{L^2(T)} \tag{B.10}$$

where $\overline{R_T}$ is denoted by $\frac{\int_T R_T dT}{vol_T}$, where $vol_T$ is the volume of the element.

Important inequalities that belong to Eqs. (B.9) and (B.10) can be deduced (Nochetto, 2006). There exist constants $C_1, C_2 > 0$ such that

$$\begin{aligned} &|||\psi - \psi_H|||^2 \leq C_1 \eta_H(\Omega)^2 \\ &C_2 \eta_H(T)^2 \leq ||\psi - \psi_H||^2_{H^1(w_T)} + osc_H(w_T)^2 \end{aligned} \tag{B.11}$$

where the energy norm is given by $|||v||| = \mathcal{B}[v,v]^{1/2}$, $\Omega$ consists of all elements and $w_T$ of all elements sharing at least one face with $T$. The first inequality tells us that the sum of the element residual and jump residual is a reliable upper bound, the latter inequality indicates that $\eta_H(T)$ is a locally sharp error estimate provided that the oscillation is small. This leads to two obvious marking strategies for a subset of elements $\hat{T}_H$ of the mesh $\mathcal{T}_H$ such that after refining, both error and oscillation are reduced. These strategies are given in Eqs. (4.4) and (4.5).

After the soil system is solved the local error indicator (Eq. (B.9)) is calculated and evaluation of the upper inequality in Eq. (B.11) indicates if refinement is needed. If so, two marking procedures can be chosen dependent on the strategy of refinement.

# References


Alm, D. M., Cavelier, J., and Nobel, P. S. (1992). A finite element model of radial and axial conductivities for individual roots: Development and validation for two desert succulents. Annals of Botany, 69, 87 – 92

Babuška, I., and W. C. Rheinboldt (1978). A posteriori error estimates for the finite element method. Int. J. Num. Methods Engin., 12, 1597–1615

Bear, J. (1972). Dynamics of fluids in porous media. American Elsevier, New york

Bristow, K.L., G.S. Campbell, and C. Calissendorf (1984). The effect of texture on the resistance to water movement within the rizosphere. Soil Sci. Soc. Am. J., 48, 266–270

Cannon, W. A. (1949). A tentative classification of root systems. Ecology, 30, 452–458

Carsel, R. F., and R. S. Parrish (1988). Developing joint probability distributions of soil water retention characteristics. Water Resources Research, 24(5), 755–769

Celia, M. A., E. T. Bouloutas, and R. L. Zarba (1990) A general mass-conservative numerical solution for the unsaturated flow equation. Water Resour. res., 26, No. 7, 1483–1496

Cheng, Y. M., and Y.H. Zhang (2007). Formulation of a Three-dimensional numerical manifold method with tetrahedron and hexahedron elements. Rock Mech. Rock Engng., DOI10.1007/s00603-006-0120-9

Clausnitzer, V., and J. W. Hopmans (1994). Simultaneous modeling of transient three-dimensional root growth and soil water flow. Plant and Soil, 164, 299–314

Coelho, E.F., and D. Or (1999). Root distribution and water uptake patterns of corn under surface and subsurface drip irrigation. Plant and Soil, 206, 123-136

Cowan, I. R. (1965). Transport of water in the soil-plant-atmosphere system. J. Appl. Ecol, 2, 221 – 239

De Jong van Lier, Q., K. Metselaar, and J. C. van Dam (2006). Root Water Extraction and Limiting Soil Hydraulic Conditions Estimated by Numerical Simulation. Vadose Zone Journal, 5, 1264-1277

De Jong van Lier, Q., and K. Metselaar (2007). The Shape of the Transpiration Reduction Function under Plant Water Stress. Vadose Zone Journal, 6, 124-139

De Willigen, P., and M. van Noordwijk (1987). Root, Plant. Production and Nutrient Use Efficiency. Ph.D. Thesis, Agricultural University, Wageningen, the Netherlands

Diggle, A. J. (1988). ROOTMAP- a model in three-dimensional coordinates of the growth and structure of fibrous root systems. Plant and Soil, 105, 169–178

Doussan, C., L. Pagès, and G. Vercambre (1998a). Modelling of the hydraulic architecture of root systems: an integrated approach to water absorption-model description. Annals of Botany, 81, 213–223

Doussan, C., G. Vercambre, and L. Pagès (1998b). Modelling of the Hydraulic Architecture of Root Systems: An Integrated Approach to Water Absorption-Distribution of Axial and Radial Conductances in Maize. Annals of Botany, 81, 225–232

Doussan, C., A. Pierret, E. Garrigues, and L. Pagès (2006). Water uptake by plant roots: II - Modelling of water transfer in the soil root-system with explicit account of flow within the root system - Comparison with experiments. Plant and soil, 283, 99–117

Dunbabin, V. M., A. J. Diggle, Z. Rengel, and R. van Hugten (2002). Modelling the interactions between water and nutrient uptake and root growth. Plant and Soil, 239, 19-38

Dunham, R. J., and P. H. Nye (1973). The influence of soil water content on the uptake of ions by roots. I. Soil water content gradients near a plane of onion roots. Journal of Applied Ecology, Vol. 10 Issue 2, 585 – 598

Frensch, J., and E. Steudle (1989). Axial and radial hydraulic resistance to roots of maize. Plant Physiol. 91, 719–726

Feddes, R.A., P. Kowalik, K. Kolinska-Malinka, and H. Zaradny (1976). Simulation of field water uptake by plants using a soil water dependent root extraction function. Journal of Hydrology, 31, 13–26

Feddes, R. A, and P.A. C. Raats (2004). Parameterizing the soil-water-plant root system, p. 95141. In RA Feddes et al. (ed.) Unsaturated-zone modeling: Progress, Challenges and Applications. Wageningen, The Netherlands

Fitter, A. H. (1996). Characteristics and functions of root systems. In Plant Roots, the Hidden Half. Eds. Y Waisel, A Eshel and U Kafkafi, p. 1–20. Marcel Dekker Inc., New York.

Gardner, W. R. (1960). Dynamic aspects of water availability to plants. Soil Sci., 89, 63–73

Garrigues, E., C. Doussan, and A. Pierret (2006). Water uptake by plant roots: I - Formation and propagation of a water extraction front in mature root systems as evidenced by 2D light transmission imaging. Plant and Soil, 283, 83–98

Green, S.R., and B.E. Clothier (1995). Root water uptake by kiwifruit vines following partial wetting of the root zone. Plant and Soil, 173, 317–328

Green, S., M. Kirkham, and B. Clothier (2006). Root Uptake and Transpiration: From Measurements and Models to Sustainable Irrigation. Agricultural Water Management, 86, 165-176

Hardelauf, H., M. Javaux, M. Herbst, S. Gottschalk, R. Kasteel, J. Vanderborght, and H. Vereecken (2007). PARSWMS: A Parallelized Model for Simulating Three-Dimensional Water Flow and Solute Transport in Variably Saturated Soils. Vadose Zone Journal, 6, 255-259

Hillel, D., C.G.E.M. van Beek, and H. Talpaz (1975). A microscopic-scale model of soil water uptake and salt movement to plant roots. Soil Science, 120, 385–399

Hillel, D. (1980). Fundamentals of soil physics. Academic Press, San Diego

Herkelrath, W.N., E.E. Miller, and W.R. Gardner (1977). Water uptake by plants. II. The root contact model. Soil Sci. Soc. Am. J., 41, 1039–1043

Huck, M.G., B. Klepper, and H.M. Taylor (1970). Diurnal variations in root diameter. Plant Physiology, 45, 529 – 530

Hunt, E. R. Jr., Running, S. W., and Federer, C. A. (1991). Extrapolating plant water flow resistances and capacitances to regional scales. Agricultural and Forest Meteorology, 54, 169-195

Hopmans, J. W., and K. L. Bristow (2002). Current capabilities and future needs of root water and nutrient uptake modeling. Adv. in Agronomy, 77, 103 – 183

Jackson, R. B., J. S. Sperry, and T. E. Dawson (2000). Root water uptake and transport: using physiological processes in global predictions. Trends in plant science: Perspectives, Vol. 5, No. 11, 482 – 488

Jakobsen, B. F. (1974). Water and phosphate transport to plant roots. Acta Agriculture Scandinavica, 24, 55–60

Jarvis, N. J. (1989). A simple empirical model of root water uptake. Journal of Hydrology, 107(1-4), 57-72

Javaux, M., T. Schröder, J. Vanderborght, and H. Vereecken (2008). Use of a Three-Dimensional Detailed Modeling Approach for Predicting Root Water Uptake. Vadose Zone Journal, 7, 1079 – 1089

Kage, H., and W. Ehlers (1996). Does transport of water to roots limit water uptake of field crops? Z. Pflanzenernähr. Bodenk., 159, 583–590

Landsberg, J. J., and N. D. Fowkes (1978). Water movement through plant roots. Annals of Botany, 42, 493–508

Leij, F. J., W. R. Russell, and S. M. Lesch (1997). Closed-form expressions for water retention and conductivity data. Ground Water, 35 (5), 848–858

Li, Y., M. Fuchs, S. Cohen, Y. Cohen, and R. Wallach (2002a). Water uptake profile response of corn to soil moisture depletion. Plant, Cell and Environment, 25, 491–500

Li, Y., R. Wallach and Y. Cohen (2002b). The role of soil hydraulic conductivity on the spatial and temporal variation of root water uptake in drip-irrigated corn. Plant and Soil, 243, 131–142

Lopez, F.B., and P.S. Nobel (1991). Root Hydraulic Conductivity of Two Cactus Species in Relation to Root Age, Temperature, and Soil Water Status. J. Exp. Bot., 42, 143–149

Mansell, R. S., L. Ma, L. R. Ahuja, and S.A. Bloom (2002). Adaptive Grid Refinement in Numerical Models for Water Flow and Chemical Transport in Soil: A Review. Vadose Zone Journal, 1, 222–238

Molz, F. J. (1981). Models of water transport in the soil-plant system: a review. Water resources research, Vol. 17, No. 5, 1245–1260

Newman, E.I. (1969). Resistance to water flow in soil and plant. I. Soil resistance in relation to amounts of root: theoretical estimates. Journal of applied Ecology, 6, 1–12

Nimah, M. N., and R. J. Hanks (1973). Model for estimating soil water, plant, and atmosphere interrelations. I. Description and sensitivity. Soil Sci. Soc. Am. Proc., 37, 522–527

Nobel, P.S., and M. Cui (1992). Hydraulic Conductances of the Soil, the Root-Soil Air Gap, and the Root: Changes for Desert Succulents in Drying Soil. J. Exp. Bot., 43, 319–326

Nochetto, R. H. (2006). Adaptive Finite Element Methods for Elliptic PDE CNA Summer School, Probabilistic and Analytical Perpectives in Contemporary PDE.

Oswald, S. E., M. Menon, A. Carminati, P. Vontobel, E. Lehmann, and R. Schulin (2008). Quantitative Imaging of Infiltration, Root Growth, and Root Water Uptake via Neutron Radiography. Vadose Zone Journal, 7, 1035 -1047

Pagès, L., M. O. Jordan, and D. Picard (1989). A simulation model of the three-dimensional architecture of the maize root system. Plant and Soil, 119, 147–154

Pagès, L., G. Vercambre, J. Drouet, F. Lecompte, C. Collet and J. Le Bot (2004). Root Typ: a generic model to depict and analyse the root system architecture. Plant and Soil, 258, 103-119

Passioura, J.B. (1980). The transport of water from soil to shoot in wheat seedlings. J. Exp. Bot., 31, 333–345

Personne, E., A. Perrier, and A. Tuzet (2003). Simulating water uptake in the root zone with a microscopic-scale model of root extraction. Agronomie, 23, 153–168

Pohlmeier, A., A. Oros-Peusquens, M. Javaux, M. I. Menzel, J. Vanderborght, J. Kaffanke, S. Romanzetti, J. Lindenmair, H. Vereecken, and N. J. Shah (2008). Changes in Soil Water Content Resulting from Ricinus Root Uptake Monitored by Magnetic Resonance Imaging. Vadose Zone Journal, 7, 1010-1017

Richards, L. A. (1931). Capillary conduction of liquids through a porous medium. Physics, Vol. 1, 318–333

Roose, T., and Fowler, A. C. (2004). A model for water uptake by plant roots. Journal of theoretical Biology, 228, 155–171

Schröder,T., M. Javaux, J. Vanderborght, and H. Vereecken (2007). Comment on "Root Water Extraction and Limiting Soil Hydraulic Conditions Estimated by Numerical Simulation". Vadose Zone Journal, 6, 524-526

Schröder, T., M. Javaux, J. Vanderborght, B. Körfgen, and H. Vereecken (2008). Effect of local soil hydraulic conductivity drop using a 3D root water uptake model. Vadose Zone Journal, 7, 1089-1098

Schröder, T., M. Javaux, J. Vanderborght, B. Körfgen, and H. Vereecken (2009). Implementation of a microscopic soil-root hydraulic conductivity drop function in a 3D soil-root architecture water transfer model. Vadose Zone Journal, *in press*

Segal, E., T. Kushnir, Y. Mualem, and U. Shani (2008). Water Uptake and Hydraulics of the Root Hair Rhizosphere. Vadose Zone Journal, 7, 1027–1034

Šimůnek, J., K. Huang, and M. Th. van Genuchten (1995). The SWMS_3D code for simulating water flow and solute transport in three-dimensional variably saturated media, V. 1.0. Research Report No. 139, U.S. Salinity Lab, ARS USDA, Riverside, Ca.

Šimůnek, J., N. J. Jarvis, M. Th. van Genuchten, and A. Gärdenäs (2003). Review and comparison of models for describing non-equilibrium and preferential flow and transport in the vadose zone. Journal of Hydrology, 272, 14–35

Somma, F., J. W. Hopmans, and V. Clausnitzer (1998). Transient three-dimensional modeling of soil water and solute transport with simultaneous root growth, root water and nutrient uptake. Plant and Soil, Vol. 202, No. 2, 281–293

Steudle, E. (2000). Water uptake by roots: effects of water deficit. J. of Exp. Botany, Vol. 51, No. 350, 1531–1542

Taylor, H.M., and B. Klepper (1975). Water uptake by cotton root systems: an examination of assumptions in the single root model. Soil Science, 120, 57–67

Tinker, P. B. (1976). Transport of water to plant roots in soil. Phil. Trans. R. Soc. Lond. B., 273, 445 – 461

Teuling, A. J., R. Uijlenhoet, F. Hupet, and P.A. Troch (2006). Impact of plant water uptake strategy on soil moisture and evapotranspiration dynamics during drydown. Geophysical Research Letters 33(3), L03401

Tsuda, M., and M. T. Tyree (2000). Plant hydraulic conductance measured by the high pressure flow meter in crop plants. J. of Exp. Botany, Vol. 51, No. 345, 823–828

Vanclooster, M., P. Viaene, J. Diels, and K. Christiaens (1996). WAVE: a mathematical model for simulating water and agrochemicals in the soil and vadose environment. Reference and user's manual. Release 2.1. Institute for Land and Water Management, KU Leuven, Belgium

Van Genuchten, M. Th. (1980). A closed-form equation for predicting the hydraulic conductivity of unsaturated soils. Soil Sci. Soc. Am. J., 44, 892–898

Weatherley, P. E. (1982). *Water uptake and flow in roots*. In: Lange O. L., Nobel P. S., Osmond C. B., Ziegler H., eds. Physiological plant ecology-II Water relations and carbon assimilation. Berlin, Springer Verlag, 79–109.

Weaver, J. E. (1958). Classification of root systems of forms of grassland and a consideration of their significance. Ecology, 39, 393–401

Wilderotter, O. (2003). An adaptive numerical method for the Richards equation with root growth. Plant and Soil, 251, 255–267

Wösten, J.H. M., G. J. Veerman, W.J. M. de Groot, and J. Stolte (2001). Waterretentie- en doorlatendheidskarakteristieken van boven- en ondergronden in Nederland: de Staringreeks. Alterra Report 153

# Acknowledgements

This thesis is a result of a joint cooperation between Jülich Supercomputing Center and ICG-4 of Forschungszentrum Jülich GmbH. On the one hand expertise was available at the applied math department of Jülich Supercomputing Center where I was appointed. On the other hand the main subject of this thesis, soil physics, is an expertise at ICG-4.

I like to thank my Promotor, and director of ICG-4, Prof. H. Vereecken who made lots of things possible, among other things an internship in the USA. Furthermore, I thank my co-promotor Prof. H. Goldbach and the director of Jülich Supercomputing Center, Prof. Th. Lippert. From ICG-4 I thank Prof. J. Vanderborght for the fruitful discussions and the awkward moments after leaving his office. A special thanks goes out to my direct mentor Prof. M. Javaux who shaped me into the scientist I am now. I hope I helped him as well in the long discussions we had: in our offices, at conferences, under lunch or at the parking lot. Furthermore, I thank my department chief of Jülich Supercomputing Center Prof. J. Grotendorst and my mentor within the math department Dr. B. Körfgen for their support over the last 3 years.

During my stay in the USA I like to thank Prof. T. Manteuffel and Prof. S. McCormick of the University of Colorado at Boulder for their enthusiasm and support in those three months.

Not only the persons who helped me professionally should be mentioned but also my fellow PhD students in Jülich Supercomputing Centre, in particular Daniel who was my roommate over the past 3 years, reminding me there is more to the drawing of one solid line resembling a root structure!

For all the stressed situations I encountered I gratefully thank my mother, especially in the early months of the thesis when her husband, my father, passed away. But not least I should thank my dearest friend Joyce. Finally, I like to thank Jana who always believed in me and had to deal with the stress at home. Hope you guys did not suffer too much!